University of Warsaw
Faculty of Physics

Tomasz Rudnicki

Student's book no.: 358844

Boer–Mulders asymmetry for the pion and Sivers asymmetry for the proton in the Drell–Yan reaction at the COMPASS experiment at CERN

second cycle degree thesis

field of study: Physics
speciality: Nuclear and Particle Physics

The thesis written under the supervision of
prof. dr hab. Barbara Badełek

Warsaw, August 2019

Oświadczenie kierujących pracą

Oświadczam, że niniejsza praca została przygotowana pod moim kierunkiem i stwierdzam, że spełnia ona warunki do przedstawienia jej w postępowaniu o nadanie tytułu zawodowego.

Data   Podpis kierujących pracą

Statement of the Supervisors on Submission of the Thesis

I hereby certify that the thesis submitted has been prepared under my supervision and I declare that it satisfies the requirements of submission in the proceedings for the award of a degree.

Date   Signature of the Supervisors:

Oświadczenie autora pracy

Świadom odpowiedzialności prawnej oświadczam, że niniejsza praca dyplomowa została napisana przeze mnie samodzielnie i nie zawiera treści uzyskanych w sposób niezgodny z obowiązującymi przepisami.

Oświadczam również, że przedstawiona praca nie była wcześniej przedmiotem procedur związanych z uzyskaniem tytułu zawodowego w wyższej uczelni.

Oświadczam ponadto, że niniejsza wersja pracy jest identyczna z załączoną wersją elektroniczną.

Data   Podpis autora pracy

Statement of the Author on Submission of the Thesis

Aware of legal liability I certify that the thesis submitted has been prepared by myself and does not include information gathered contrary to the law.

I also declare that the thesis submitted has not been the subject of proceedings resulting in the award of a university degree..

Furthermore I certify that the submitted version of the thesis is identical with its attached electronic version.

Date   Signature of the Author of the thesis

Abstract

This thesis describes studies of the Drell–Yan data collected in 2015 by COMPASS experiment at CERN. The main goals of the analysis were: extraction of the first moment of the Boer–Mulders function for the pion and extraction of the weighted Sivers transverse spin asymmetry for the proton. Furthermore, the performance of the COMPASS spectrometer during 2018 data–taking periods was analyzed. The first moment of the Boer–Mulders function $h_1^{\perp(1)}(x)$ weakly decreases with increasing values of x. The obtained value of the $A_T^{sin\Phi_S \frac{q_T}{M_\pi}} = 0.025 \pm 0.079$ is compatible with zero within 1 σ statistical uncertainty and thus excludes any physics conclusions regarding the Sivers transverse spin asymmetry. Due to a low statistics the uncertainties of the presented results are large. Analyses of the COMPASS data collected in 2018 that can improve precision of the results are going on.

Key words

Parton Distribution Functions, Drell-Yan, Transverse Spin Asymmetry, Boer-Mulders, Sivers, COOOL plots, COMPASS, CERN, Deep Inelastic Scattering

Area of study

13.2 Physics

Tytuł pracy w języku polskim

Asymetria Boer–Muldersa dla pionu i asymetria Siversa dla protonu w reakcji Drella–Yana w eksperymencie COMPASS w CERN

Streszczenie

Praca opisuje badanie reakcji Drella–Yana oparte o dane zebrane w 2015 roku przez eksperyment COMPASS w CERN. Głównymi celami analizy były: otrzymanie pierwszego momentu funkcji Boer–Muldersa dla pionu oraz ważonej asymetrii Siversa dla protonu. Ponadto naszkicowane są studia wydajności spektrometru COMPASS podczas zbierania danych w 2018 roku. Pierwszy moment funkcji Boer–Muldersa $h_1^{\perp(1)}(x)$ słabo maleje z rosnącymi wartościami x. Otrzymana wartość asymetrii Siversa $A_T^{sin\Phi_S \frac{q_T}{M_\pi}} = 0.025 \pm 0.079$ jest zgodna z zerem w granicy 1 σ niepewności statystycznej i tym samym wyklucza fizyczne konkluzje dotyczące asymetrii Siversa. W związku z małą statystyką niepewności prezentowanych rezultatów są duże. Analizy danych zebranych przez COMPASS w 2018 roku, które mogą poprawić precyzję rezultatów, trwają.

Contents

List of Figures

List of Tables

Chapter 1

Introduction

1.1. Quark Parton Model

In 1964, following a discovery of several tens of "elementary particles", Gell-Mann and Zweig postulated the Quark Model [1, 2] which stated that all hadrons are composed of three quarks (up, down, strange). In 1967 the SLAC experiment published the results of the inelastic scattering of the electron beam on the proton, Fig. 1.1. The results showed a weak dependence of the cross-section on the negative square of the four-momentum (Q^2) transferred between the colliding particles. This phenomenon was explained by the Parton Model [3] of R. Feynman in 1969. He postulated, as it was summarized by Bjorken and Paschos, that the electron-proton scattering can be interpreted as a "quasi-free scattering from point-like constituents within the proton, as viewed from the frame where proton has infinite momentum" [4].

In 1970s the quarks proposed by Gell-Mann and Zweig were interpreted as the partons and two models combined into the Quark Parton Model (QPM). Later three more quarks were discovered and added to the model: the charm (1974), bottom (1977) and top (1995). In the early 1970s the QPM was expanded by the ideas of the Quantum Chromodynamics (QCD), theory that describes the strong interactions which binds the quarks inside of the nucleus.

The QCD states that the exchange particle for the strong interactions is a gluon. The gluon was discovered by the DESY experiment at the electron-positron collider PETRA in 1979 [6]. In the final state of the electron-positron annihilation three jets were observed. Two of them were a manifestations of the production of the quark-antiquark pair and the third one was a manifestation of the gluon, see Fig. 1.2.

In this thesis we are trying to further expand our knowledge about the structure of the nucleon and of the pion, based on the data collected by the COMPASS experiment at CERN in 2015.

1.2. Deep Inelastic Scattering

Most experiments that probe the nucleus inner structure employ the Deep Inelastic Scattering (DIS). The DIS occurs when a part of the energy of the incoming particle is transferred to the constituents of the target particle. The result of this process is a break up of the target particle and a production of new particles:

$$l(k) + H(P) \rightarrow l(k') + X, \tag{1.1}$$

where H denotes the initial hadron, l and l' the incoming and outgoing leptons, respectively, and X stands for the produced particles. Letters in the parentheses denote the four-momenta
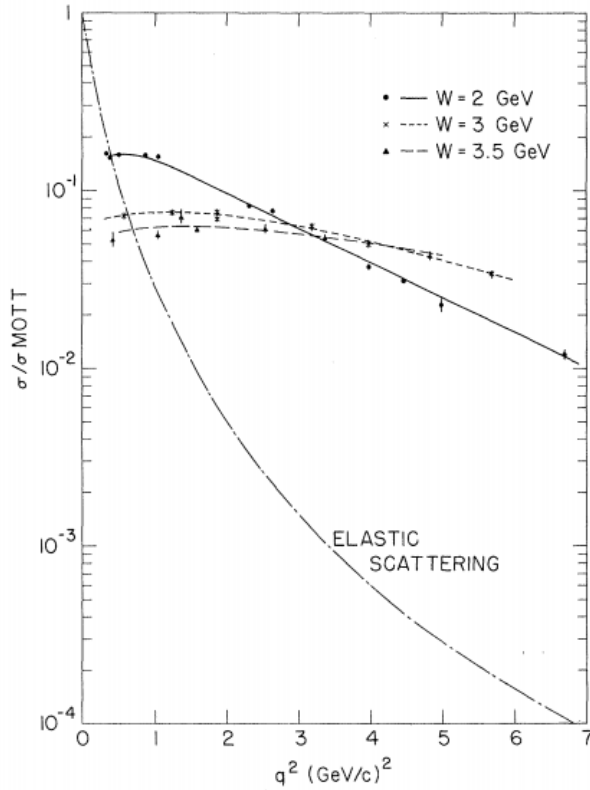
Figure 1.1: Cross section for the deep inelastic scattering (normalised to the Mott cross section) as a function of Q^2 [5]. W is an invariant mass of the recoiling target system.
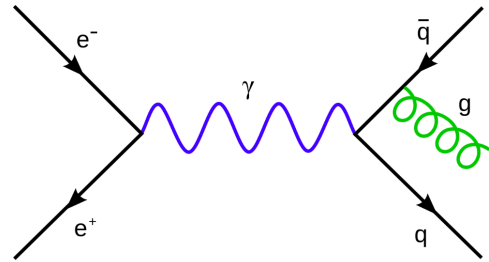
Figure 1.2: The Feynman diagram of the electron-positron annihilation process with the quark-antiquark pair and gluon in the final state.

of the corresponding particles. In Fig. 1.3 a diagram of the deep inelastic scattering of the electron on the proton is shown. In this example in the leading order the exchanged particle (γ^*) is the virtual photon but it can also be the bosons Z^0 or $W^\pm$ for higher center of mass energies.
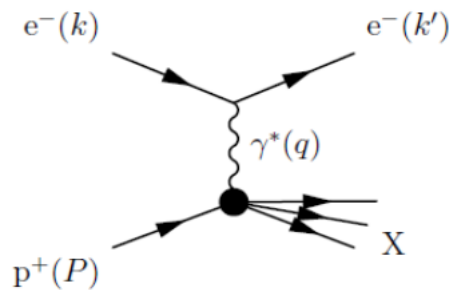
Figure 1.3: The lowest order of the Feynman diagram of the DIS.

The deep inelastic scattering of the incoming particle (beam particle) on the stationary target is commonly described by the following variables (the last equation in each formula

corresponds to the laboratory frame):

$$Q^2 \equiv -q^2 = -(k - k')^2 = -2m^2 - 2pp'cos\theta + 2EE', \tag{1.2}$$

$$x \equiv \frac{Q^2}{2Pq} = \frac{Q^2}{2M_B\nu}, \tag{1.3}$$

$$y \equiv \frac{Pq}{Pk} = \frac{\nu}{E}, \tag{1.4}$$

$$\nu = \frac{Pq}{M_B} = E - E' \tag{1.5}$$

where m denotes the lepton mass, M_B is the mass of the target particle, E and E' denote energies of the incoming and outgoing lepton in the laboratory reference frame (LAB), respectively, θ is the angle of the scattered lepton in the LAB, p and p' are the magnitudes of the momenta of the incoming and outgoing lepton in the LAB, respectively.

The variable x ('Bjorken x') characterizes an elasticity of the scattering; it can take values in the range between 0 and 1 and in case of an elastic scattering it is equal to 1. In the frame where $|\boldsymbol{P}| \to \infty$ the x variable can be interpreted as the fraction of the target particle momentum carried by the parton struck by the γ^*.

The deep inelastic scattering can be divided into two categories: inclusive DIS and semi-inclusive DIS (SIDIS). Inclusive DIS is a process in which only a scattered lepton is detected in the final state. In the SIDIS we detect at least one of the produced particles.

1.3. Parton Distribution Functions

Results of the SLAC experiment forced physicists to create new tools for description of the nucleon inner structure. The Parton Distribution Functions (PDFs) are one of them. They can be interpreted as a probability of finding a parton with the momentum $x\boldsymbol{P}$ in the particle with the momentum $\boldsymbol{P}$ in the frame where $|\boldsymbol{P}| \to \infty$.

The cross-section of the inelastic electron–proton scattering that was measured by the SLAC experiment can be described in terms of two independent variables as:

$$\frac{d\sigma}{dxdQ^2} = \frac{4\pi\alpha^2}{Q^4} \left[\left(1 - y - \frac{M_Bxy}{2E} \right) \frac{F_2(x,Q^2)}{x} + y^2 F_1(x,Q^2) \right] \tag{1.6}$$

where $F_1(x,Q^2)$ and $F_2(x,Q^2)$ denote nucleon structure functions and α is the fine structure constant. In the leading order (LO) of the perturbative QCD the Parton Distribution Functions $q_i(x,Q^2)$ are linked with the cross-section of the inelastic scattering by the structure functions:

$$F_2(x,Q^2) \overset{\mathrm{LO}}{=} x \sum_i e_i^2 q_i(x,Q^2) \tag{1.7}$$

The example of the current status of knowledge on PDFs of the proton is shown in Fig. 1.4. Years of studies led to precise results with the small uncertainties for $x \gtrsim 10^{-3}$. For comparison in Fig. 1.5 the current constraints for the PDFs of the pion and the best fits to the data are shown. The constraints were provided by the NA3 experiment [7], and the fits are the results of two PDF analyses of the data. The goal of this thesis is further expansion of the knowledge on pion PDFs.
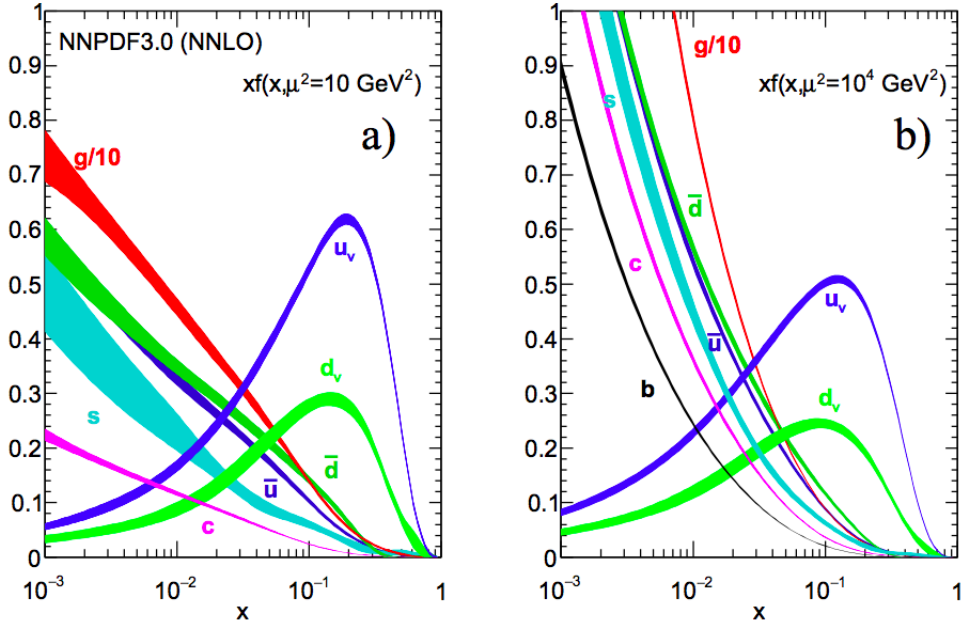
Figure 1.4: Example of the current status of knowledge on PDFs of the proton for two values of Q^2 (denoted in the picture as μ^2) in the NNLO of the perturbative QCD [8].
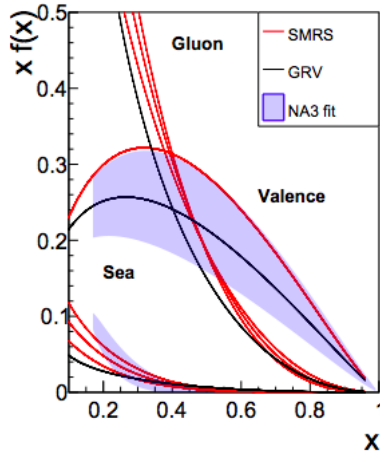
Figure 1.5: Current status of knowledge on PDFs of the pion. The shaded (purple) areas denote constraints provided by the NA3 experiment [9]. Lines correspond to the QCD data analyses: SMRS and GRV.

1.4. Transverse momentum-dependent parton distribution functions

The PDFs described in the previous section are averaged over the spin of the partons and they are very often referred to as the unpolarized PDFs (in the following the explicit Q^2

4

dependence will be neglected for clarity):

$$f_1 \equiv q^{\uparrow}(x) + q^{\downarrow}(x), \tag{1.8}$$

where $q^{\uparrow}$ denotes the density of the quarks with the spin parallel and $q^{\downarrow}$ the quarks with the spin anti-parallel with respect to the spin of the longitudinally polarized particle (the particle spin is parallel or anti–parallel with respect to the beam momentum).

One of the issues that emerged after introduction of the parton spin is the proton spin puzzle discovered by the European Muon Collaboration (EMC) in 1987 [10]. It was expected that the quarks carry all the proton spin but the EMC results show that the quarks spin contribute only to about one third of the total spin of the nucleon.

In the collinear approximation of QCD a nucleon structure can be described by three PDFs. One of them (the unpolarized PDF f_1) is described above and two others are the helicity and the transversity distributions:

$$g_{1L} \equiv q^{\uparrow}(x) - q^{\downarrow}(x) \tag{1.9}$$

$$h_1 \equiv q_T^{\uparrow}(x) - q_T^{\downarrow}(x) \tag{1.10}$$

The subscript T denotes the transverse polarization of the nucleon. In the relativistic formalism the helicity and transversity distributions are not equal.

Taking into accout the transverse momentum of the parton $\boldsymbol{k_T}$ the nucleon spin structure can be described by 8 Transverse Momentum Dependent (TMD) Parton Distribution Functions: $f_1(x, \boldsymbol{k_T^2})$, $g_{1L}(x, \boldsymbol{k_T^2})$, $h_1(x, \boldsymbol{k_T^2})$, $g_{1T}(x, \boldsymbol{k_T^2})$, $h_{1T}^{\perp}(x, \boldsymbol{k_T^2})$, $h_{1L}^{\perp}(x, \boldsymbol{k_T^2})$, $h_1^{\perp}(x, \boldsymbol{k_T^2})$ and $f_{1T}^{\perp}(x, \boldsymbol{k_T^2})$. The QCD-TMD approach is applicable for $\boldsymbol{k_T^2} \ll Q^2$. First three of the TMD-PDFs integrated over $\boldsymbol{k_T^2}$ give the already discussed unpolarized PDF ($f_1(x)$), the helicity distribution ($g_{1L}(x)$) and the transversity distribution ($h_1(x)$). The rest vanish after integration over $\boldsymbol{k_T}$. Last two of them which are T-odd and are called Boer-Mulders and Sivers functions, respectively, will be of particular interest in this thesis. In Fig. 1.6 all the TMDs and their dependence on the nucleon spin, parton spin and transverse momentum $\boldsymbol{k_T}$ are shown.

In this work we focus on T-odd TMDs: Boer-Mulders and Sivers functions. T-odd functions are process–dependent which means their signs depend on the reaction they were extracted from:

$$h_1^{\perp}(\text{SIDIS}) = -h_1^{\perp}(\text{DY}) \tag{1.11}$$

$$f_{1T}^{\perp}(\text{SIDIS}) = -f_{1T}^{\perp}(\text{DY}) \tag{1.12}$$

The Boer-Mulders function describes the correlation between the transverse spin and the transverse momentum of the quark within an unpolarized nucleon. The Sivers function denotes the correlation of the transverse spin of the nucleon and the transverse momentum of the quark.

The Boer-Mulders function is one of the transversity distributions that are the chiral-odd functions so their measurements require two flips of the quark chirality. Such behaviour is strongly suppressed in the inclusive DIS process but can occur in the Drell-Yan process (DY) with two hadrons in the initial state or the semi-inclusive DIS with one hadron in the initial and at least one in the final state. This thesis focuses on the analysis of the DY process.

1.5. Drell-Yan process

The Drell-Yan process occurs when a quark of one of colliding hadrons annihilates with an antiquark of another hadron. In this process a virtual photon γ^* (or a boson Z^0) is created
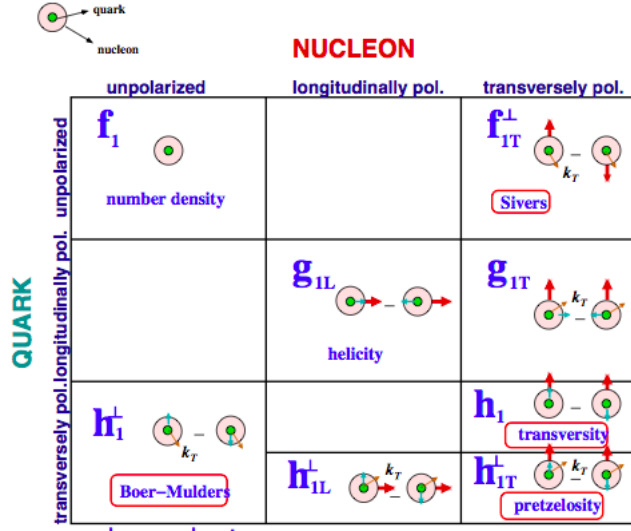
Figure 1.6: All TMD PDFs of the nucleon after taking into account nucleon spin, parton spin and transverse momentum of the parton. The red bold arrows indicate nucleon spin and the green arrows indicate the parton spin.
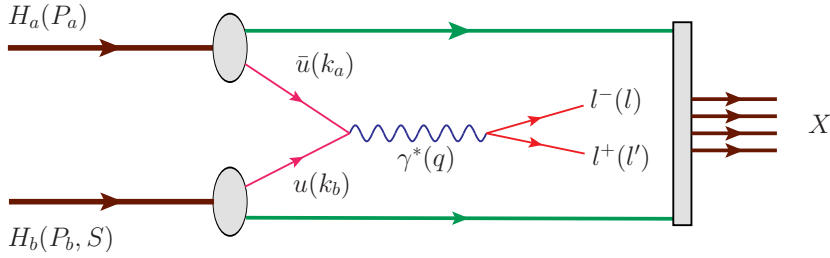
Figure 1.7: The Feynman diagram of the Drell-Yan process. The quark-antiquark pair annihilates creating the virtual photon which in turn gives into the oppositely charged leptons pair. S denotes a spin of the b hadron. Figure taken from [11].

which then gives a pair of oppositely charged leptons:

$$H_A(P_A) + H_B(P_B) \rightarrow l(k) + \bar{l}(k') + X. \tag{1.13}$$

Formation of the boson Z^0 is strongly suppressed for energies lower than its mass. In the above equation $H_{A,B}$ denote incoming hadrons, l and l' outgoing leptons, X undetected particles; letters in the parentheses denote the particles four-momenta, see Fig. 1.7. The unpolarized Drell-Yan process greatly helped in determination of the pion PDFs and still plays an important role in the experimental physics but nowadays more attention attracts the polarized version of the process. Great advantage of the latter is a possibility of the measurement of the TMDs and that almost the whole energy of the colliding partons may transform into the mass of electromagnetic force carrier which provides an opportunity for production of the particles with higher masses. Unfortunately it also has a low counting rate which makes it more demanding experimentally [12].

There are two convenient reference frames for description of the DY process [11]:
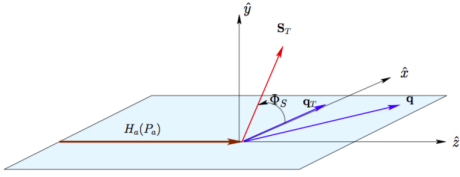
Figure 1.8: Definition of the azimuthal angle Φ_S of the transverse target spin in the Target Rest Frame [11].
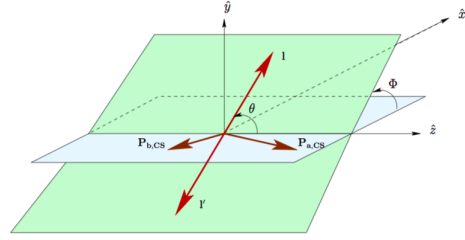
Figure 1.9: Definition of the polar and azimuthal angles θ and Φ of the lepton momentum in the Collins-Soper frame [11].

1. Target Rest Frame (TRF) is defined by the $\hat{z}$ axis along the particle beam momentum, $\hat{x}$ axis along the transverse momentum of the virtual photon $\boldsymbol{q_T}$ and $\hat{y} = \hat{z} \times \hat{x}$ (Fig. 1.8).

2. Collins-Soper Frame (CS) is the rest frame of the virtual photon (see Fig. 1.9). It can be reached from the TRF by two consecutive boosts - first along the $\hat{z}$ axis and second along the $\hat{x}$ axis that the virtual photon momentum $\boldsymbol{q}$ vanish.

The general Drell-Yan cross section and thus the asymmetries described in the following chapter depend on the angles defined above[1].

1.6. Weighted asymmetries and the first moment of the Boer–Mulders function

The T-odd functions described in this thesis (Boer-Mulders, Sivers) are hard to detect because they are tiny but in the LO of the QCD the quark densities can be expressed by asymmetries that are easier to measure. Generally a spin asymmetry A can be defined as:

$$A = \frac{N^{\uparrow\uparrow} - N^{\uparrow\downarrow}}{N^{\uparrow\uparrow} + N^{\uparrow\downarrow}} \tag{1.14}$$

where $N^{\uparrow\uparrow}$ denotes a number of the events with the spin of the incoming particle parallel to the spin of the target particle and $N^{\uparrow\downarrow}$ denotes a number of the events with the spin of the incoming particle anti-parallel to the spin of the target particle.

The general form for the Drell-Yan cross section when only a target nucleon is transversely polarized is expressed by six spin asymmetries [13]. One of them is the Sivers weighted transverse spin asymmetry (TSA) defined as:

$$A_T^{sin\Phi_S W_{\Phi_S}}(x_\pi, x_N) = \frac{\int d^2\boldsymbol{q_T} W_{\Phi_S} F_T^{sin\Phi_S}}{\int d^2\boldsymbol{q_T} F_U^1}, \tag{1.15}$$

where x_π and x_N are the fractions of longitudinal momenta of the pion and proton carried by the colliding partons, F_U^1 denotes the target polarization independent structure function, $F_T^{\sin\Phi_S}$ is the transverse polarization dependent structure functions and W_{Φ_S} is an event weight. The advantage of using weights is that the convolutions of the transverse momentum dependent (TMD) parton distribution functions (PDFs), which are present in the standard

---

[1]In the analysis the angles Φ and Φ_S are often denote as ϕ and ϕ_S, respectively.

interpretation of the Drell–Yan cross-sections [12] and consequently in the standard transverse spin asymmetries (TSAs), are replaced by the products of the transverse moments of the TMDs.

The first moment of the Boer–Mulders function defined as [14, 15]:

$$h_1^{\perp(1)}(x) = \int \mathrm{d}^2 \boldsymbol{k_T} \, \frac{\boldsymbol{k_T^2}}{2M^2} h_1^{\perp}(x, \boldsymbol{k_T^2}), \tag{1.16}$$

where $h_1^{\perp}(x, \boldsymbol{k_T^2})$ is the Boer–Mulders TMD PDF. The extraction is carried out using the formula for the weighted Boer–Mulders asymmetry defined as [16]:

$$\begin{aligned}
A_{\mathrm{T}}^{\sin(2\phi-\Phi_S)\frac{q_{\mathrm{T}}}{M_\pi}}(x_\pi, x_N) &= -2 \frac{\sum_q e_q^2 \left[h_{1,\pi}^{\perp(1)\bar{q}}(x_\pi) \, h_{1,\mathrm{p}}^q(x_N) + (q \leftrightarrow \bar{q}) \right]}{\sum_q e_q^2 \left[f_{1,\pi}^{\bar{q}}(x_\pi) \, f_{1,\mathrm{p}}^q(x_N) + (q \leftrightarrow \bar{q}) \right]} \\
&\approx -2 \frac{e_{\mathrm{u}}^2 \, h_{1,\pi}^{\perp(1)\bar{\mathrm{u}}}(x_\pi) \, h_{1,\mathrm{p}}^{\mathrm{u}}(x_N)}{\sum_{q=\mathrm{u,d,s}} e_q^2 \left[f_{1,\pi}^{\bar{q}}(x_\pi) \, f_{1,\mathrm{p}}^q(x_N) + (q \leftrightarrow \bar{q}) \right]},
\end{aligned} \tag{1.17}$$

where q runs over quark flavours, $f_1^{\bar{q}}(x_\pi)$ and $f_1^q(x_N)$ are the unpolarised PDFs of the pion and proton, $h_{1,\mathrm{p}}^q$ is the transversity PDF of the proton, and $h_{1,\pi}^{\perp(1)\bar{q}}$ is the first transverse moment of the Boer–Mulders function of the pion. Due to a very poor knowledge of the Boer–Mulders and transversity PDFs of the quark sea, these functions are assumed to be zero. Indeed the quark sea transversity extracted from the available data is compatible with zero.

The unpolarized PDFs of the proton are very well known and the parametrizations of the unpolarized PDFs of the pion can be found in the literature. The Boer–Mulders asymmetry was measured by COMPASS in 2015 and values of the transversity PDF of the proton were extracted from COMPASS data. Thus after simple transformation of the Eq. (1.17) we obtain formula for the first transverse moment of the Boer–Mulders function which is one of the two goals of this thesis.

In this thesis, we present the extraction of the first moment of the Boer–Mulders function (Chapter 4) and the Sivers asymmetry (Chapter 5). A non-zero Sivers asymmetry for the nucleon may point towards a non-zero parton angular momentum, a missing piece in the nucleon spin puzzle. The first moment of the Boer–Mulders function is one of the characteristic charges that can describe the pion structure.

Chapter 2

COMPASS experiment

The Common Muon and Proton Apparatus for Structure and Spectroscopy (COMPASS) is a fixed-target experiment at the M2 beam line of the Super Proton Synchrotron (SPS) at the European Laboratory for Particle Physics, CERN. It was proposed in 1996 and its goal is the investigation of a hadron structure and a hadron spectroscopy, which are both manifestations of the non-perturbative QCD [17]. In 2012, the physics data-taking entered the second phase (COMPASS II) expanding the original scientific goals of the experiment.

In the second phase of the data-taking COMPASS collected among others the data of the Drell-Yan reaction colliding the hadron beam with the transversely polarized target. The hadron beam consists of the pions, kaons and protons with the energy up to 280 GeV/c and is produced in the collisions of the proton beam extracted from the SPS with the primary production target. At 190 GeV/c negative hadron beam consists of 95% pions, 4.5% kaons and 0.5% antiprotons whereas positive hadron beam consists of 71.5% pions, 25.5% protons and 3.0% kaons [18].

The momentum and the angular acceptances of the hadron beam are defined during a collimation process [19]. Due to a relatively low counting rate of the Drell-Yan process the high intensity beam is required. In COMPASS the highest available hadron beam intensity of about 10^8 particles per second is limited only by the radioprotection requirements.

COMPASS polarized target for the Drell-Yan studies consists of two oppositely polarized cells, each 55 cm long and 2 cm in diameter. Protons of the target material (NH_3) can reach polarization of about 80-90% using the dynamic nuclear polarization (DNP) method [20]. After the DNP process the target is rapidly cooled down below 100 mK. At this temperature a relaxation time of the proton polarization is longer than 1000 hours.

The M2 beam line and COMPASS spectrometer were constructed in the way that allows measurement of both the DY process and the semi-inclusive DIS. This creates a unique opportunity for the measurement of the Boer-Mulders and the Sivers effects in both processes at the same facility.

COMPASS spectrometer is divided into two stages: the large angle spectrometer (LAS) and the small angle spectrometer (SAS) that are built around the dipole magnets (SM1, SM2) and ensure ± 180 mrad and ± 30 mrad polar acceptances, respectively. Both spectrometer stages consist of tracking detectors, an electromagnetic calorimeter, a hadronic calorimeter and a muon filter. The LAS is additionally equipped with a ring imagining Cherenkov (RICH) counter for the charged particles identification. In Fig. 2.1 a three-dimensional view of the spectrometer setup for the Drell-Yan process is shown. Upstream of the target two differential Cherenkov counters that identify hadrons present in the hadron beam are located.

In Chapter 3 the analysis of the performance of the COMPASS spectrometer is provided.
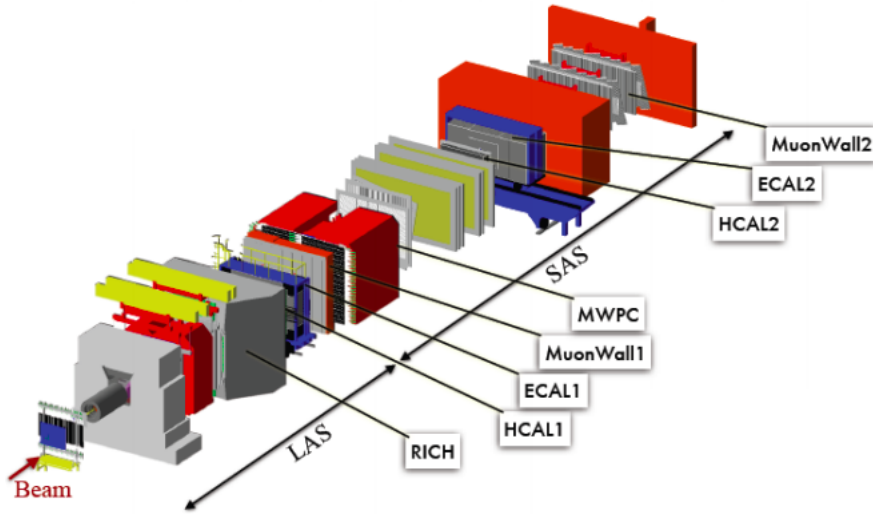
Figure 2.1: COMPASS spectrometer setup for the Drell-Yan process. The beam comes from the left side [16].

For better understanding of that chapter a short principle of operation of all the detectors is decribed in the following sections.

2.1. Target region

The target region consists of the target itself and surrounding equipment necessary for the DNP process, see Fig. 2.2. Downstream of the target the hadron absorber is located. It is needed during collecting of the Drell-Yan data in order to keep the occupancy in the next detectors at an acceptable level. It also reduces background from the pions which would decay into a pair of muons. Aluminum and tungsten plugs inside the hole in the center of the hadron absorber stop the beam that did not interact with the target.

2.2. Tracking system

The tracking system consists of a few detectors adapted for different tasks. Near the beam the tracks are detected by Scintilating Fibres (SciFi) that have a spacial resolution $\sigma_s \approx 130$ μm and a time resolution $\sigma_t \approx 0.4$ ns. At larger angles the tracks are recorded by the Micromegas (micromesh gaseous structure) and the GEMs (gas electron multipliers) with a spatial resolution $\sigma_s \approx 70$ μm and a time resolution $\sigma_t \approx 12$ ns [16]. Both detectors have a dead zone, 5 cm in diameter, in the middle.

Largest angles are covered by multi-wire proportional chambers (MWPCs), straw drift tubes (Straws) and drift chambers (DC). Dead zones of the MWPCs are 16-22 cm in diameter depending on the distance from the target. Three drift chambers are located in the LAS with dead zones 30 cm in diameter. The SAS contains eight drift chambers of different sizes and active areas. Downstream of the RICH a detector consisting of the mini drift tubes (MDTs) with 1×0.5 m^2 central dead zone is located. The straw station is positioned in the middle of the spectrometer and its dead zone is 20×20 cm^2. A 'tracking station' consists of detectors

① He-3 precooler	⑥ 80 K Thermal radiation shields		
② Microwave cavity	⑦ 4.2 K Thermal radiation shields		
③ Target cells	⑧ Dilution refrigerator		
④ Target holder	⑨ He-4 gas-liquid separator		
⑤ Magnets	⑩ Pulse tube cryocooler		
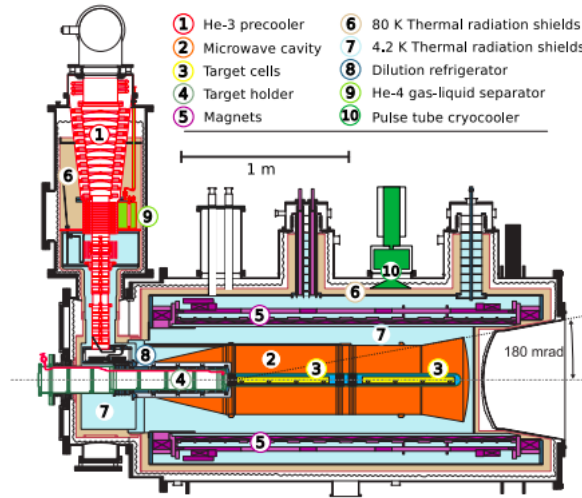
Figure 2.2: Side view of the NH$_3$ target region [16].

of the same type located approximately at the same distance from the target along the beam axis.

2.2.1. Scintilating fibres

The SciFi detectors provide tracking of all charged particles in and very near the center of the beam axis. Passage of a particle creates a light in the scintillating material that is read by photon detectors. A group of channels that measure horizontal or vertical coordinate of the track is referred to as X- and Y-plane, respectively. U- and V-plane denote planes that measure the track projection onto the axis rotated about 45° clockwise and anticlockwise, respectively, with respect to the $\hat{x}$-axis. The $\hat{x}$-axis points at the Jura mountains, $\hat{z}$-axis is directed along the beam and the direction of $\hat{y}$ makes the coordinate system right-handed.

In order to provide a sufficient number of photo-electrons each detector plane consists of a few overlapping layers of fibres shifted with respect to each other, see Fig. 2.3. Tracks are reconstructed based on the time correlation between signals read from the overlapping layers only. The tracks of the incoming particle and the scattered particle are also linked by the time correlation.

2.2.2. Micromegas

The Micromega principle of operation is based on an ionization caused by a particle passing between parallel electrode plates. A special feature of this detector is a metallic micromesh betweeen the electrodes. An ionization takes places in the conversion gap with the field about 1 kV/cm, see Fig. 2.4. In the amplification gap where the field value reaches about 50 kV/cm an avalanche of electron/ion pairs is produced.

An advantage of the Micromega detector is a short drift time in the amplification gap (about 100 ns). Most of the ions from the avalanche are captured by the field near the mesh and do not drift back to the conversion gap. A time resolution of COMPASS Micromegas is optimized by using a Ne/C$_2$H$_6$/CF$_4$ gas mixture (80%/10%/10%). The detector has a dead zone, 5 cm in diameter, in the middle.

Figure 2.3: Configuration of the scintilator fibre layers. The actual number of the layers vary from 4 to 14 depending on the station [18].

Figure 2.4: Principle of operation of the Micromega detector [18].
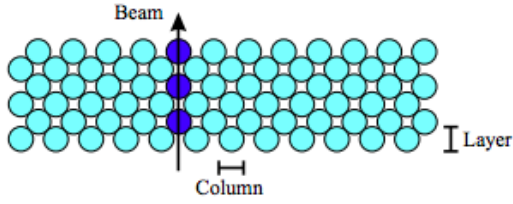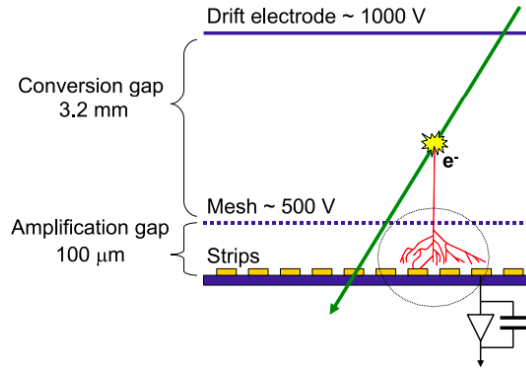
2.2.3. GEMs

The GEMs consists of a 50 μm thin Polyimide foil covered with copper on both sides. The copper layer has many micro–holes of 70 μm in diameter (about 104 holes/cm^2). Primary electrons drifting into the holes are multiplied by the several potential difference across the foil when the foil is inserted into a gas-filled chamber. The electrons from the holes are extracted by an electric field to the next amplification stage or to the readout anode.

COMPASS GEM detectors consists of three amplification layers stacked on top of each other, see Fig. 2.5. The readout channels are segmented into two perpendicular layers. Each GEM detector record two projections of the particle position with a strongly correlated amplitudes that reduce ambiguities in multi-hit events.

2.2.4. Drift chambers

Each drift chamber station consists of eight layers of the wires in 4 planes. U- and V-plane are rotated by $\pm 20°$ with respect to the $\hat{x}$-axis. The planes order (XYUV) was chosen in order to minimize a fake tracks reconstruction.

Each DC layer consists of 176 sensitive wires of 20 μm in diameter and 177 potential wires of 100 μm in diameter and is enclosed within two Mylar cathode foils of 25 μm thickness covered with 10 μm of graphite, see Fig. 2.6. A charged particle going through the gas produces electrons that drift to the closest sensitive wire and thus create a signal.

COMPASS uses three identical DC stations - one upstream and two downstream of the SM1. The drift chambers were optimized for operation upstream of the first dipole magnet (SM1) where the total flux is higher by almost three orders of magnitude compared to the downstream side of the SM1.

2.2.5. Multi-wire proportional chambers

Principle of operation of the MWPC is the same as the principle of operation of the drift chamber, except that in case of the drift chambers the time of drift of the electron is registered and provides additional information about the tracks.

There are 3 types of the MWPCs. Type-A detectors have three layers - one in X-plane and 2 rotated by about $\pm 10°$ with respect to the vertical axis creating U- and V-plane. Type-A* detectors have additional fourth layer in the Y-plane. Type-B detectors have only two layers
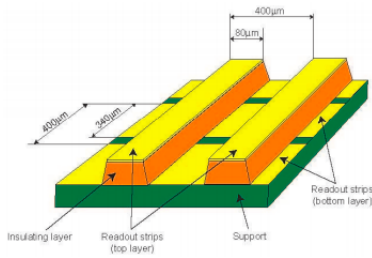
Figure 2.5: Scheme of the GEM detector readout system [18].
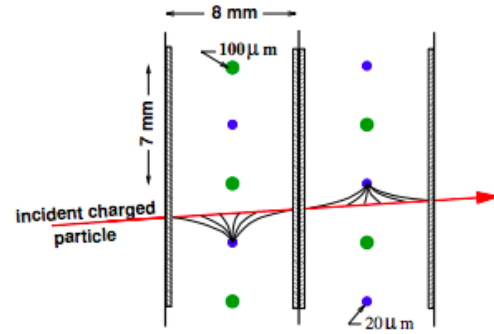
Figure 2.6: Principle of operation of the drift chamber detector [18].
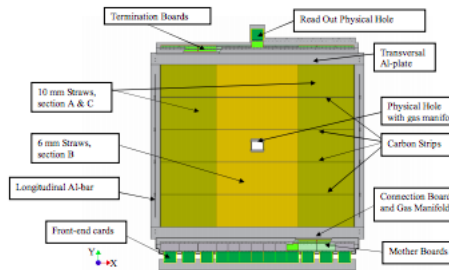
Figure 2.7: Scheme of the straw detector (type X) [18].

- vertical and tilted (U or V) one. Type-B stations are composed of two detectors rotated by 90° with respect to each other.

2.2.6. Straw tube chambers

The straws consist of two Kapton layers - the inner layer of 40 μm thickness glued onto the aluminum foil of 12 μm thickness. The counting gas is supplied through the end-plugs and the gas-manifold integrated into the detector structure. The gold-plated tungsten anodes with 30 μm diameter are centered in the straw tubes by two end-plugs and four small plastic spacers, see Fig 2.7.

Each detector consists of two staggered layers of the straws glued onto the aluminum plate for mechanical stability. The straw detectors have a dead zone in the center of about 20×20 cm^2, part of which is a rectangular hole without any material of about 20×10 cm^2. Because the straws measure the three-dimensional trajectory of a particle each straw station consists of three detectors: X-, Y- and U-plane. The X- and U-planes have slightly different geometry than the Y-plane.

2.3. Particle identification

In the analysis of the Drell-Yan process it is necessary to identify the muons coming from the collision vertex, see Fig. 1.7. In COMPASS the muons are identified as the only particles that penetrate through the 'muon walls'. Their tracks can be extrapolated down to the
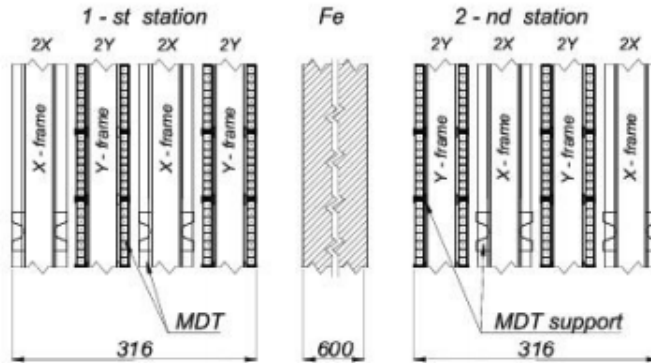
Figure 2.8: Sketch of the muon wall [18]. All dimensions are given in milimeters. MDT denotes mini drift tubes.

collision vertex. Though very useful in other analyses the information from RICH detector is not used in the Drell-Yan analysis even if it is present in the spectrometer setup during the Drell-Yan data taking.

2.3.1. Muon walls

The 'muon walls' consist of two detector stations separated with the 60 cm thick iron absorber. Each station is build of four detectors with two gaseous wire detectors (MDTs) from both sides. The detectors in each station record x- or y-coordinate of the particle position, alternately (Fig. 2.8). The outer surfaces of each station are covered with the 1 mm aluminium sheet for mechanical, electrostatic and noise protection. All the particles except the muons are stopped inside the muon walls which simplifies the particle identification process.

2.3.2. Ring-imagining Cherenkov detector

The Ring-imagining Cherenkov detector principle of operation is based on the measurement of the presence and characteristics of the Cherenkov radiation emitted by a charged particle passing through a transparent refractive medium. The RICH detector vessel is filled with a C_4F_{10} radiator gas. Hadrons going through the vessel emit photons that are reflected by the 21 m^2 surface covered with the mirrors, divided into two spherical surfaces. The photons are detected by the multi-wire proportional chambers located outside of the detector acceptance area. The beam is separated from the vessel by 5 cm diameter steel pipe.

Pattern recognition allows for determination of the most relevant Cherenkov parameters: number of photons per event, Cherenkov angle and Cherenkov angle resolution. The minimum value of the angle resolution is equal to 0.5 mrad and allows the pions and kaons separation at 2.5 σ level up to 43 GeV/c. In Fig. 2.9 an example of an event reconstruction is shown.

2.4. Trigger system

The trigger system is designed to provide a signal for the readout electronics to record an event. A decision is made based on the veto detectors and the energy loses in calorimeters. In COMPASS there are two types of the calorimeter detectors: hadron (HCAL) and
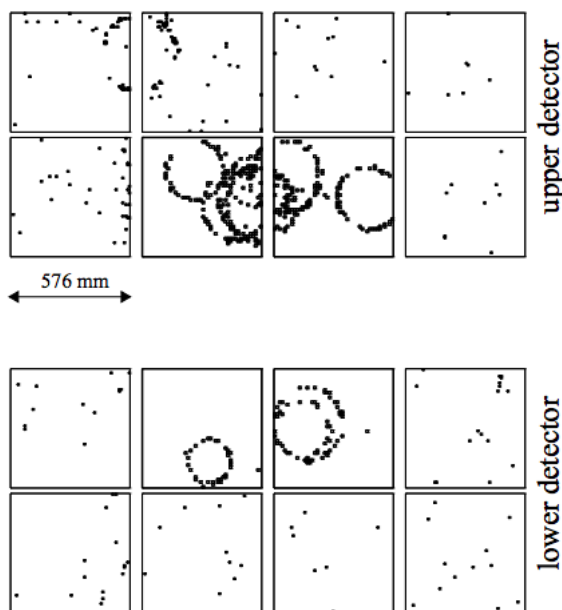
Figure 2.9: Example of an event reconstruction in the RICH detector [19].

electromagnetic (ECAL) ones. All veto detectors use a scintillation process to detect particles.

2.4.1. Electromagnetic calorimeters

COMPASS sprectrometer contains two electromagnetic calorimeters: ECAL1 and ECAL2. Their task is to measure the energy of the gamma rays and the electrons that develop an electromagnetic shower inside the lead glass of the calorimeters. Electrons and positrons on their way through the glass emit a Cherenkov light that is proportional to the energy deposited in each counter.

Both ECALs are mounted on platforms that can be moved vertically and horizontally which is used during the spectrometer calibration process. Both of them have also a hole in the center for the beam passage. Each lead glass is viewed at the end by a photomultiplier tube (PMT) that measures an amount of the emitted light, see Fig. 2.10.

2.4.2. Hadron calorimeters

The hadron calorimeters (HCALs) have a modular structure, each module consists of 40 layers of the iron and scintillator plates. Both of them are the sampling calorimeters and serve a double purpose: they measure energy of hadrons produced in the beam–target collision and participate in the triggering on inelastic muon scattering events. In Fig. 2.11 the structure of the HCAL module is shown.

2.4.3. Sandwich veto detector

A sandwich veto detector vetoes events in which photons or charged particles get out of the LAS acceptance. The detector consists of five layers of the steel-covered lead plates and of the scintillators, Fig. 2.12. With Monte Carlo simulations the detector efficiency was determined to be higher than 95% for the pions with the energies larger than 50 MeV.
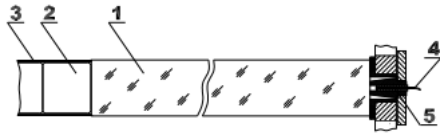
Figure 2.10: Scheme of the ECAL2 detector: 1 is a TF1-000 lead glass radiator, 2 is a FEU-84-3 PMT, 3 denotes a permalloy magnetic screen, 4 is a quartz fibre to distribute the light pulse of the monitoring system and 5 denotes a light guide connector [18].
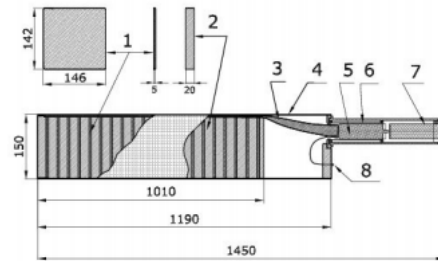
Figure 2.11: Structure of the HCAL1 module: 1 are scintillators, 2 are iron plates, 3 is a light guide, 4 is a container, 5 denotes a PMT, 6 is a PMT magnetic shielding, 7 denoters a Cockcroft-Walton divider and 8 is an optical connector for LED control. All dimensions are given in milimeters [18].
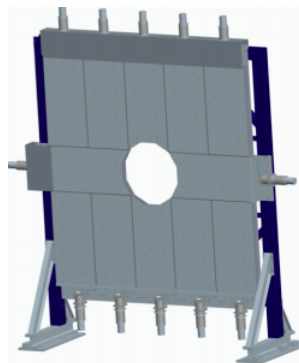
Figure 2.12: Scheme of the sandwich veto detector [19].

Chapter 3

COOOL plot analysis

The COMPASS data quality and stability is checked through the COOOL plot analysis, where COOOL stands for the COMPASS Object Oriented OnLine monitoring program. Information that is recorded by incorrectly working detectors are excluded from other COMPASS analyses. In this thesis we describe the analysis that was carried on by the author on the data recorded in 2018. Results were produced in the format of list of the incorrectly working detector channels. Analyzed was data collected by 69 COMPASS detectors during more th an 3500 runs.

3.1. Data acquisition system

A typical COMPASS hadron beam intensity of 5×10^7 particles per second indicates a total trigger rate of more than 30 kHz. The overall number of electronic channels of more than 250 000 and the mean event size of 40 kB combine to a total amount of up to 580 TB data recorded per year. Accordingly, a data rate of up to 1.2 GB/s is acquired during the 9.6 s long SPS spill. The high rate of the data flow requires almost a dead-time free readout scheme, Fig. 3.1.

3.2. Detector monitoring system

In order to provide a high quality data the COMPASS spectrometer has to be constantly under control. The data flow system (read-out chain, front-end electronics, stability of the beam characteristics and trigger counting rate) are monitored online but it is not enough to ensure the stability and consistency of the recorded data.

Additional tools provided by user interface for monitoring of the COMPASS apparatus allow a closer look into more specific detector parameters (hit profiles, time or amplitude information or supplied voltages and currents). These parameters are analyzed during the data taking as well as offline before the data production process. The latter denotes a raw data analysis when the first loose cuts are imposed on the data (e.g. trigger requirements).

The SPS provides the proton beam in bunches that create packs of the secondary hadron beams called spills. 200 consecutive spills make a 'run'. Runs recorded for about a week with the same target polarization form a 'sub-period'. A 'period' is formed by two or more consecutive sub-periods that contain about the same amount of the recorded data but with opposite target polarizations.
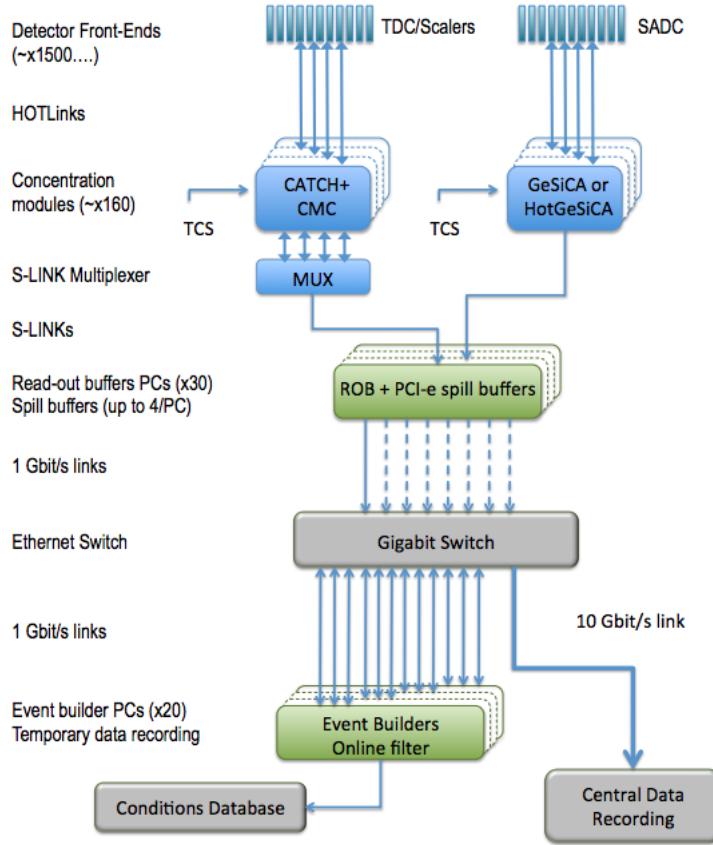
Figure 3.1: Schematic view of the data acquisition system (DAQ) of the COMPASS experiment [19].

3.3. Detector time profile

In Fig. 3.2 example of the detector hit profile is shown. The abscissa shows the channel number and the ordinate corresponds to the number of hits per channel in a given run. Detector stability can be checked by comparing number of hits per channel along the data taking period. In order to do this effectively the detector time profiles are created, Fig. 3.3. The abscissa shows the run number and the ordinate corresponds to the channel number.

The black vertical line divides the period into the sub-periods following the convention of the COMPASS experiment. In Fig. 3.4 division of periods into sub-periods is shown, for each sub-period a target polarization is given. Duration of the period was chosen such that the data taking process was optimized (approximately the same numbers of events in both parametrization orientations).

3.4. Run selection

During data taking only events that fulfill trigger requirements are recorded. Thus it happens that runs with no data recorded are saved by the DAQ (e.g. when spills are empty). Such runs have to be excluded from further analysis. The following criteria were used for run selection:
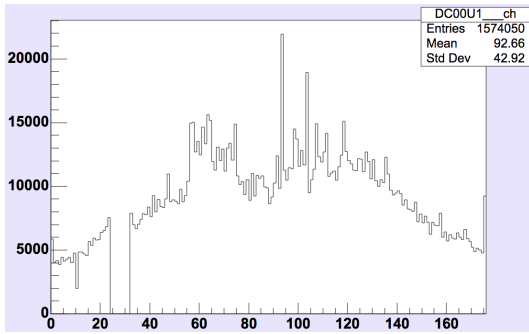
Figure 3.2: Example of the detector hit profile, here for drift chambers: the rate of the hits recorded per channel in a given run. The abscissa shows the channel number.
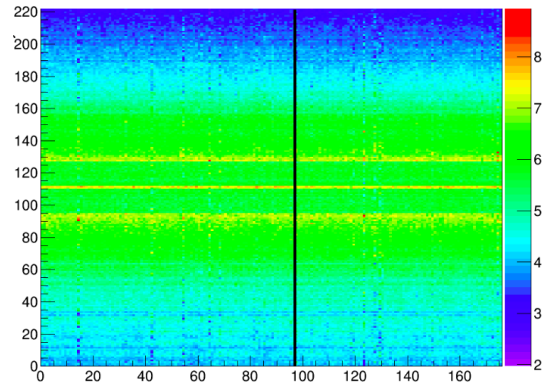
Figure 3.3: Example of the detector time profile, here for straws. The abscissa shows the run number and the ordinate corresponds to the channel number.

- A file with the detector profiles (i.e. a detector hit profile) has to exist.

- Data from at least 10 not empty spills have to be recorded.

- Number of particles detected during a run is larger than 5% of the mean number of particles detected per run during a given data taking period.

Runs that fulfill these conditions are part of the list of the runs that will be analyzed during the production process.

3.5. Zero clusters

To provide a high quality of the recorded data a list of the incorrectly working detectors is created. Instabilities in the detector performance are later taken into account during the analyses (i.e. while estimating detector acceptance). A high number of the detector channels working simultaneously makes it impractical to analyze each channel stability separately. Therefore the following procedure was adopted.

The first step of the detector stability check is searching in the detector time profile for the 'zero clusters'. They are neighboring channels that did not record data in a few consecutive runs. They manifest themselves as empty areas on the detector time profile of at least 100 empty pixels where each empty pixel corresponds to a channel that for the whole run did not record any data.

An area is called zero cluster if it fulfills the following conditions:

- At least five out of 15 consecutive channels are dead.

- Channels were dead for at least 10 out of 30 consecutive runs.

In Figures 3.5 and 3.6 examples of zero clusters visible on the detector time profiles are shown. Each detected zero cluster is treated individually depending on the whole detector performance.

19
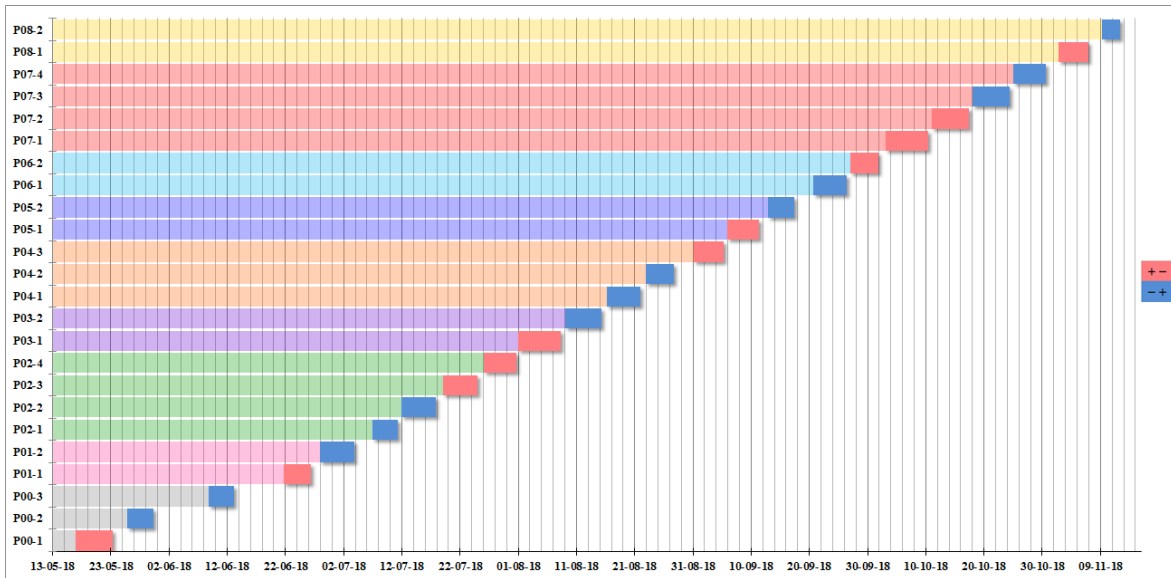
Figure 3.4: Division of the data taking periods into the sub-periods and the target polarization per sub-period.
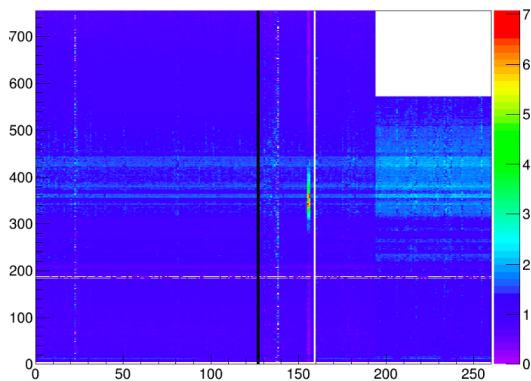
Figure 3.5: Example of a zero cluster, here for a multi-wire proportional chamber.
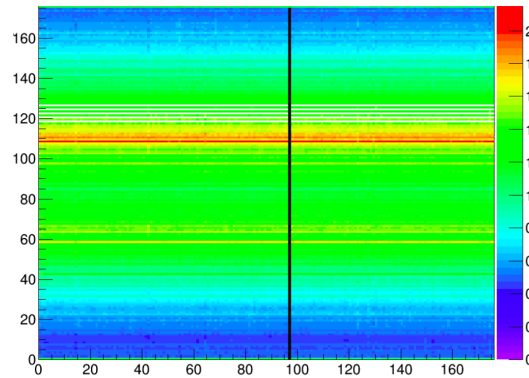
Figure 3.6: Example of the zero cluster created by not neighboring channels, here for drift chambers.

3.6. Hot channels

Another technical issue that can be detected by the detector time profile analysis is an unstable performance of the readout electronics. It is detected as an abnormal amount of the data recorded by the channel (hot channel). In Fig. 3.5 an example of the hot channels (red-green area) is shown.

3.7. Example of the rejection process

In this section we provide a few examples of the detector time profiles for a data taking period P5 in 2018. All unstable channels were excluded from further analyses for the whole or the part of the period as written under the figures.
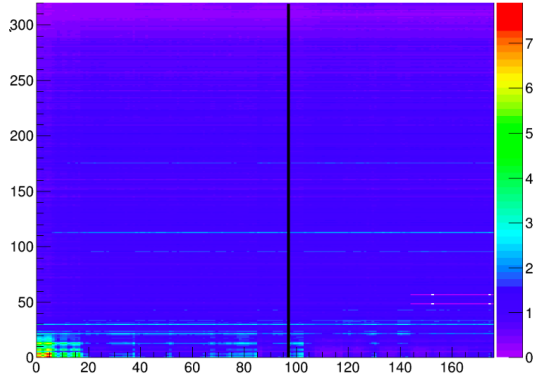
Figure 3.7: Unstable performance of the drift chamber channels from 1 to 30 - excluded for the whole period.
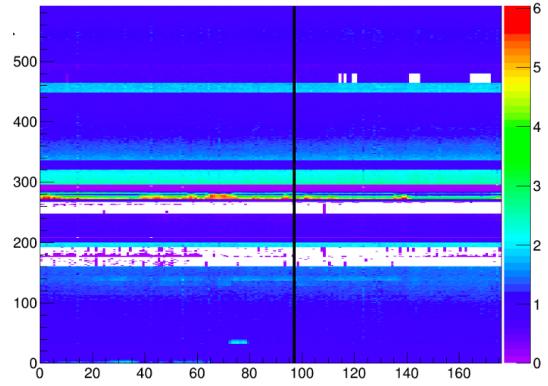
Figure 3.8: Channels of the RICH wall from 160 to 200 (zero cluster) and from 245 to 280 (zero cluster and hot channels) excluded for the whole period.
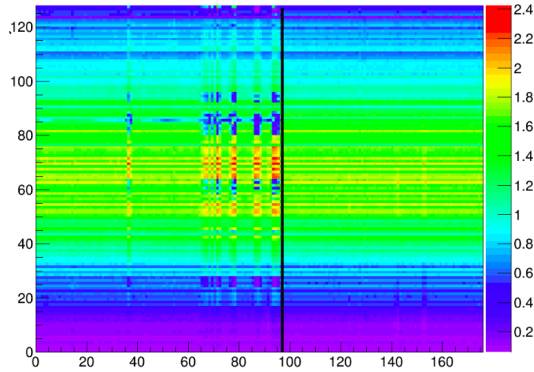
Figure 3.9: Unstable performance of the whole scintillating fibres detector during 30 consecutive runs - excluded for runs between 62 and 92.
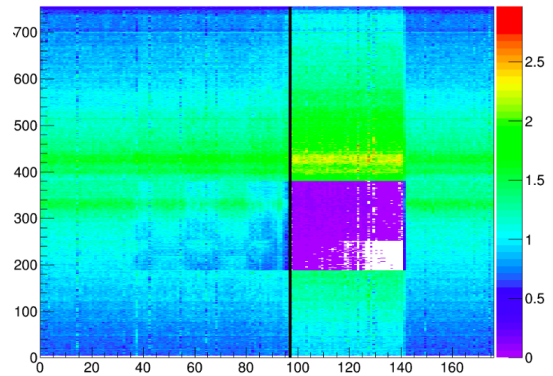
Figure 3.10: An unstable multi-wire proportional chamber detector performance in the 1st half of the 2nd sub-period. Symmetric exclusion of the whole detector for 90 runs around the 1st run of the 2nd sub-period.

Chapter 4

Extraction of the first moment of the Boer-Mulders function for the pion

4.1. Weighted asymmetry approach

Besides PDFs, the pion structure can be described by its characteristic charges. One of them that can be extracted from the COMPASS data is the first moment of the Boer-Mulders function. For its extraction we used the weighted transverse spin asymmetries. Advantage of using weights is that the convolutions of the TMD PDFs, which are present in the standard TSAs, are replaced by products of the transverse moments of the TMDs. The weighted asymmetries were previously used in the context of the SIDIS [14, 15, 21, 22].

For extraction of the first moment of the Boer-Mulders function we used the Eq. (1.17) and the values of the Boer–Mulders asymmetry weighted with q_T/M_π, $A_T^{sin(2\phi-\phi_s)\frac{\boldsymbol{q_T}}{M_\pi}}$, measured by COMPASS, see Fig. 4.1 and Tab. 4.1. As mentioned in Sec. 1.6 the contribution of the Boer–Mulders and transversity PDFs of the quark sea is neglected. In addition, we consider only u, d and s quarks in the denominator of Eq. (1.17). All the quantities remaining on the right hand side of that equation, except for the first transverse moment of the Boer–Mulders function $h_{1,\pi}^{\perp(1)}$, can be found in the literature.

Table 4.1: Average values of the kinematic variables used during extraction of the first moment of the Boer–Mulders function for the pion $h_{1,\pi}^{\perp(1)}$.

| x_π	x_N	Q^2 $(\mathrm{GeV}/c)^2$	$A_T^{sin(2\phi-\phi_s)\frac{\boldsymbol{q_T}}{M_\pi}}$	σ_A
0.315	0.2136	25.4	-2.943	1.2380
0.477	0.1662	29.7	-0.348	1.2980
0.689	0.1349	33.9	-1.283	1.2240

4.2. Input data for the analysis: unpolarised and transversity PDFs

Parametrization of the unpolarised PDFs of the pion $f_{1,\pi}(x_\pi)$ and the proton $f_{1,p}(x_N)$ were taken from the GRV-PI pion PDF [25] and the CTEQ 5D proton PDF [26] in the LHAPDF library [27]. In Figs 4.2 and 4.3 the unpolarised PDFs at the scale $Q^2 = 25$ $(\mathrm{GeV}/c)^2$, which
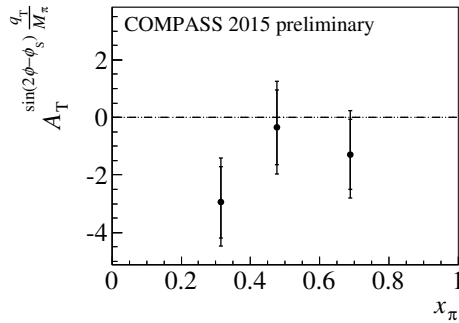
Figure 4.1: The measured $\sin(2\phi - \phi_S)$ asymmetry weighted with q_T/M_π as a function of x_π. The longer bars combine statistical and systematic errors in quadrature [23]. Figure taken from [24].
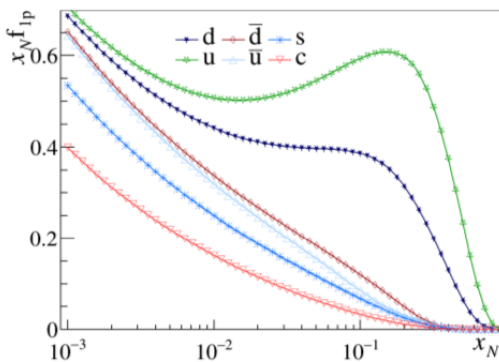
Figure 4.2: LO parametrization of the unpolarized PDFs of the proton as a function of x_N at $Q^2 = 25$ $(\text{GeV}/c)^2$ [26]. Figure taken from [24].
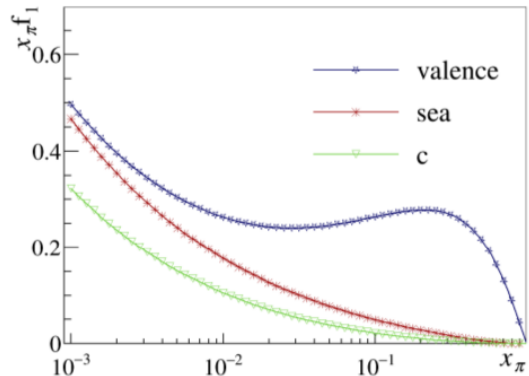
Figure 4.3: LO parametrization of the unpolarized PDFs of the pion as a function of x_π at $Q^2 = 25$ $(\text{GeV}/c)^2$ [25]. Figure taken from [24].

is close to the average scale of COMPASS Drell–Yan experiment, are shown. In this work the values of the PDFs, at the mean x and Q^2 values, calculated separately for each x_π bin were taken. The valence pion PDF depends on the x_π bin, as can be seen in Fig. 4.4. On the other hand, the proton PDFs are almost constant in the three bins, as the average x_N does not change much (see Tab. 4.1).

The proton transversity PDF $h^u_{1,p}(x_N)$ has been extracted by several groups. To obtain it in a simple way, we utilize a point-by-point extraction from COMPASS data [29]. The Q^2 of the transversity changes from point to point and in our range of x_N between 0.1–0.3 it lies between 8 and 23 $(\text{GeV}/c)^2$. Changes within the Drell-Yan kinematics were neglected. Proton transversity values were fitted with a function:

$$h^u_{1,p}(x_N) = a \frac{x_N^b (1 - x_N)^c}{B(b+1, c+1)}, \tag{4.1}$$

where a, b, and c are the fit parameters and $B(b+1, c+1)$ is the beta function that should

23
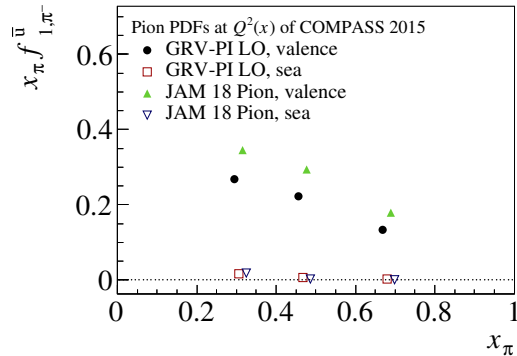
Figure 4.4: Pion PDFs evaluated in the bins of x_π. JAM 18 Pion denotes parametrization proposed by the JAM Collaboration [28] and the GRV-PI of the Ref. [25]. Figure taken from [24].

decrease a correlation between the parameter a and remaining parameters:

$$B(b+1, c+1) = \int_0^1 \mathrm{d}t \, t^b (1-t)^c. \tag{4.2}$$

We parametrized independently the two sets of the $h_{1,\mathrm{p}}^{\mathrm{u}}(x_N)$ data which were extracted in Ref. [29] using two asymmetries - the Collins asymmetry and the dihadron asymmetry. In the latter set we fix the value of the c parameter to fulfill a condition:

$$\lim_{x_N \to 1} h_{1,\mathrm{p}}^{\mathrm{u}}(x_N) = 0.$$

The fits of $h_{1,\mathrm{p}}^{\mathrm{u}}(x_N)$ do not distinguish between the above two data sets, see Fig. 4.5. In Fig. 4.6 the parametrization of the Collins asymmetry measurement is shown. Values of the fit parameters in this case are:

$$a = 0.081 \pm 0.061 \qquad b = 1.302 \pm 0.65 \qquad c = 3.5 \pm 4.3,$$
$$\mathrm{corr}(a, b) = -0.82 \qquad \mathrm{corr}(a, c) = -0.95 \qquad \mathrm{corr}(b, c) = 0.94.$$

The uncertainty bands of the $h_{1,\mathrm{p}}^{\mathrm{u}}(x_N)$ fit function are constructed using the the covariance matrix of the fit and the standard error propagation technique. The values of the $h_{1,\mathrm{p}}^{\mathrm{u}}(x_N)$ used to calculate the first moment of the Boer–Mulders function for the pion $h_{1,\pi}^{\perp(1)}$ are given in Tab. 4.2 in bins of x_N and x_π. Average values of these variables and Q^2 are given.

4.3. Results

The first moment of the Boer–Mulders function for the pion $h_{1,\pi}^{\perp(1)}$ extracted from Eq. 1.17 is shown in Figs 4.7 and 4.8. On the plots two sets of error-bars are marked at each point: statistical and combined in quadrature. The latter takes also into account the systematic error of the weighted asymmetry. The values of the first moment of the Boer-Mulders function $h_{1,\pi}^{\perp(1)}$ with the combined errors $\sigma_h^{(1)}$ are shown in Tab. 4.2.
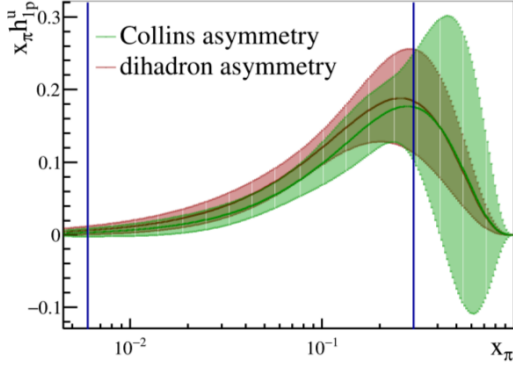
Figure 4.5: Comparison of the best fits of the transversity extracted from the Collins and the dihadron asymmetries in Ref. [29]. Figure taken from [24].
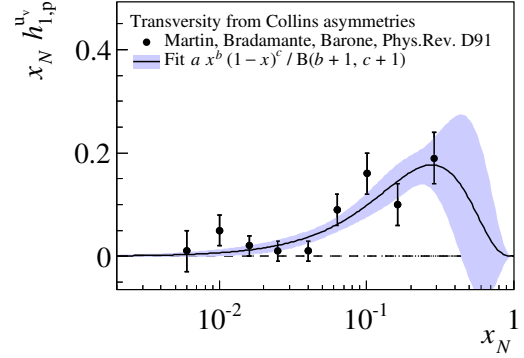
Figure 4.6: Fit of the proton transversity extracted from the Collins asymmetries in Ref. [29]. Figure taken from [24].
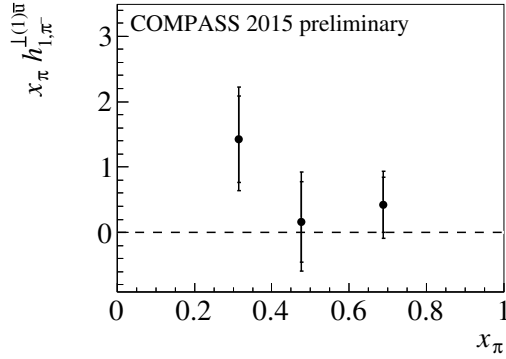
Figure 4.7: The extracted first transverse moment of the Boer–Mulders function of the pion $h_{1,\pi}^{\perp(1)}$ as a function of x_π. Unpolarized pion PDF $f_{1,\pi}(x_\pi$ is from Ref. [25]. Figure taken from [24].
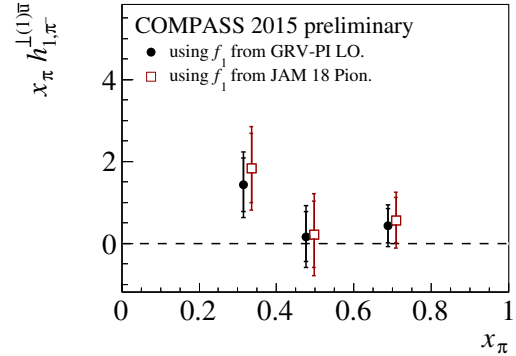
Figure 4.8: Same as in Fig. 4.7 but for two different parametrizations of the unpolarized pion PDF $f_{1,\pi}(x_\pi)$, Refs [25] and [28]. Figure taken from [24].

Table 4.2: Kinematic variables x_π x_N Q^2 $(\text{GeV}/c)^2$, weighted asymmetry $A_T^{sin(2\phi-\phi_s)\frac{q_T}{M_\pi}}$, transversities $h_{1,p}^{u}$ obtained from the fit of Ref. [29] data and values of the first moment of the Boer-Mulders function $h_{1,\pi}^{\perp(1)}$ in each kinematic bin.

x_π	x_N	Q^2 $(\text{GeV}/c)^2$	$A_T^{sin(2\phi-\phi_s)\frac{q_T}{M_\pi}}$	σ_A	$h_{1,p}^{u}$	σ_h	$h_{1,\pi}^{\perp(1)}$	$\sigma_h^{(1)}$
0.315	0.2136	25.4	-2.943	1.2380	0.1675	0.0323	1.4292	0.6614
0.477	0.1662	29.7	-0.348	1.2980	0.1472	0.0324	0.1644	0.6145
0.689	0.1349	33.9	-1.283	1.2240	0.1270	0.0301	0.4245	0.4173
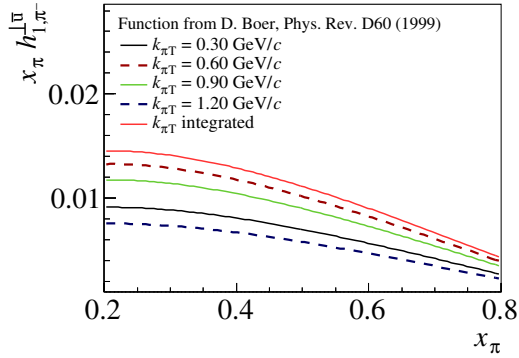
Figure 4.9: The Boer–Mulders function parametrization Eq. 4.3 [30] as a function of x_π for different $k_{\pi T}$. Figure taken from [24].
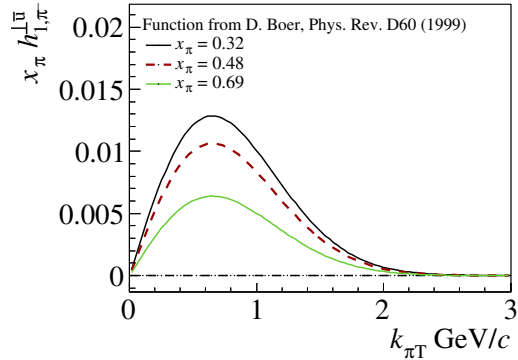
Figure 4.10: The Boer–Mulders function parametrization [30] plotted against $k_{\pi T}$ for different values of x_π. Figure taken from [24].

The results obtained in this thesis are compared with the only available theoretical prediction of Ref. [30]. To this aim the Boer–Mulders function parametrized there as:

$$h_{1,\pi}^{\perp\bar{u}}(x_\pi, \boldsymbol{k}_{\boldsymbol{\pi T}}^2) = \frac{\alpha_T}{\pi}\, c_\pi^{\bar{u}}\, \frac{M_C M_\pi}{\boldsymbol{k}_{\boldsymbol{\pi T}}^2 + M_C^2}\, e^{-\alpha_T \boldsymbol{k}_{\boldsymbol{\pi T}}^2}\, f_{1,\pi}(x_\pi), \tag{4.3}$$

was used. Here the parameters $M_C = 2.3\,\text{GeV}$, $\alpha_T = 1\,\text{GeV}^{-2}$ and $c_\pi^{\bar{u}} = 1$ are fixed by a fit to NA10 Drell–Yan data [31]. After substitution of the two components of the $\boldsymbol{k}_{\boldsymbol{\pi T}}$ vector with $k_{\pi T}$, ϕ_k and integration over the azimuthal angle ϕ_k the function reads:

$$h_{1,\pi}^{\perp\bar{u}}(x_\pi, k_{\pi T}^2) = 2 k_{\pi T}\, \alpha_T\, c_\pi^{\bar{u}}\, \frac{M_C M_\pi}{k_{\pi T}^2 + M_C^2}\, e^{-\alpha_T k_{\pi T}^2}\, f_{1,\pi}(x_\pi). \tag{4.4}$$

This function is shown in Fig. 4.9 and 4.10. The integral of the $h_{1,\pi}^{\perp\bar{u}}(x_\pi, \boldsymbol{k}_{\boldsymbol{\pi T}}^2)$ (Eq. 4.3) over $\boldsymbol{k}_{\boldsymbol{T}}$, $k_{\pi T}$ integrated, is shown in the first figure as well.

The first moment of the Boer–Mulders function is calculated according to the Eq. 1.16 as:

$$h_{1,\pi}^{\perp(1)\bar{u}}(x_\pi) = \frac{\alpha_T\, c_\pi^{\bar{u}}\, M_C}{M_\pi}\, f_{1,\pi}(x_\pi) \int_0^\infty \mathrm{d}k_{\pi T}\, \frac{k_{\pi T}^3}{k_{\pi T}^2 + M_C^2}\, e^{-\alpha_T k_{\pi T}^2}, \tag{4.5}$$

which is an integral without analytical solution. Integrating numerically, a comparison to our results shown in Fig. 4.11 was obtained. Within large experimental errors the curve reproduces the behaviour of measurements.

4.4. Systematic checks

In this section a few systematic checks made on the obtained $h_{1,\pi}^{\perp(1)}$ values are discussed. Dependence of choices of the unpolarized PDF of the pion $f_{1,\pi}$ and the proton $f_{1,p}$ on the error of the $h_{1,\pi}^{\perp(1)}$ values is checked. Compatibility of our parametrization of the proton transversity $h_{1,p}^u$ with the only available theoretical prediction [30] is checked.
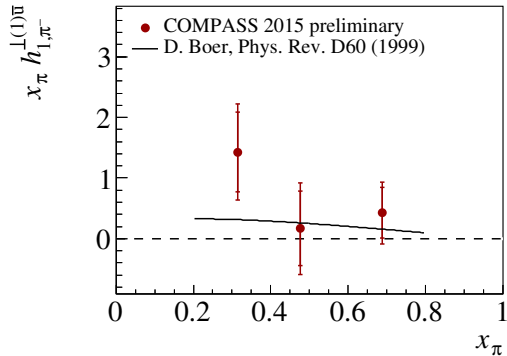
Figure 4.11: Results of this analysis (points). Inner error-bars are statistical and the outer are combined in quadrature. The curve is a result of theoretical predictions [30]. Figure taken from [24].
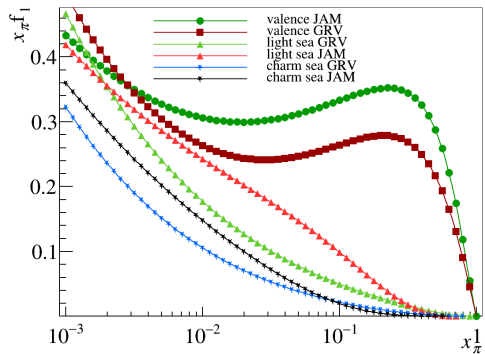
Figure 4.12: Spin-independent PDFs for the pion, $x_\pi f_1$ as functions of x_π at $Q^2 = 25\,(\text{GeV}/c)^2$ from the two analyses: GRV-PI pion PDF [25] and JAM pion PDF [28]. Figure taken from [24].

Proton unpolarised PDF: When instead of the CTEQ5 parametrization of the proton unpolarized PDF $f_{1,p}$ the more recent CT-14 LO PDF set [32] is used, the result is systematically lower by about 4 %, which is much below the level of both the statistical precision and other sources of systematic uncertainties. This contribution to the systematic error of $h_{1,\pi}^{\perp(1)}$ was thus neglected.

Pion PDF: The results dependence on the unpolarized PDF of the pion $f_{1,\pi}$ parametrization was checked using the Jefferson Lab Angular Momentum (JAM) parametrization of $f_{1,\pi}$ [28]. In Fig. 4.12 both the pion PDFs parametrizations for $Q^2 = 25\,(\text{GeV}/c)^2$ are shown. Comparison of the results obtained with the GRV-PI and the JAM PDFs is shown in Fig. 4.13. Within large experimental uncertainties the results on $h_{1,\pi}^{\perp(1)}$ do not show any sensitivity to $f_{1,\pi}$.

Proton transversity PDF: As was pointed out before, the result does not change much when one uses the dihadron-based instead of the Collins-based transversity from Ref. [29]. We have not tried to use the results of other extractions. In Ref. [29] the result is compared to and found compatible with, for example, a work published in Ref. [33] (Fig. 4.14). One can note that the uncertainty band of Ref. [33] is wider than the band given by our fit.

27

Figure 4.13: Comparison of the final result dependence on the proton transversity and the unpolarized pion PDF parametrizations [25, 28]. Figure taken from [24].

Figure 4.14: Comparison of the used proton transversity (points) with the parametrisation from Ref. [33] at scale $Q^2 = 10\,(\mathrm{GeV}/c)^2$. Figure taken from [24].

Chapter 5

Extraction of the Sivers asymmetry for the proton

5.1. Weighted Sivers TSA

The comparison of the weighted Sivers TSA $A_T^{sin\phi_S \frac{\mathbf{q_T}}{M_\pi}}$ defined in Eq. 1.15 measured in SIDIS and Drell-Yan 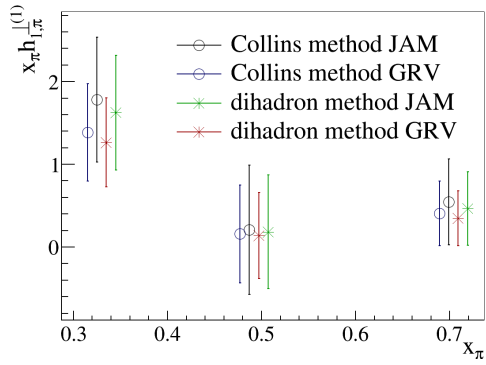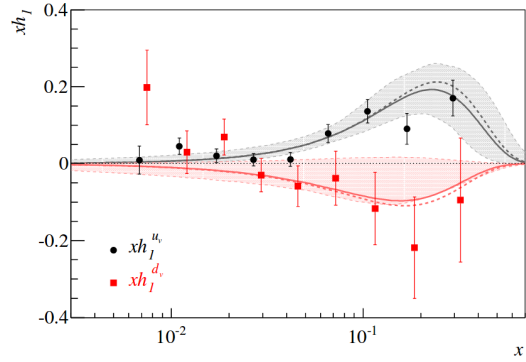processes has been proposed [34] as the easiest way to check the validity of (TMD QCD) predictions, Eqs (1.11–1.12). Moreover the non–zero Sivers asymmetry may indicate a non–zero parton angular momentum in the proton, a quality very difficult to access otherwise.

In Eq. 1.15 the weight is chosen such that it provides easy interpretation of the integral in the numerator of the right hand side of the Equation. The integrals are represented as (see Ref [23] for the details):

$$\int d^2\mathbf{q_T} F_U^1 = \frac{1}{N_c} \sum_q e_q^2 [f_{1,\pi}^{\bar{q}}(x_\pi) f_{1,p}^q(x_N) + (q \longleftrightarrow \bar{q})], \tag{5.1}$$

$$\int d^2\mathbf{q_T} \frac{q_T}{M_p} F_T^{sin\phi_S} = \frac{2}{N_c} \sum_q e_q^2 [f_{1,\pi}^{\bar{q}}(x_\pi) f_{1T,p}^{\perp(1)q}(x_N) + (q \longleftrightarrow \bar{q})], \tag{5.2}$$

where $N_c = 3$ is the number of colour charges, M_p is the mass of the proton and the $f_{1T,p}^{\perp(1)}$ is the first moment of the Sivers TMD PDF for the proton.

The important part of the extraction of the Sivers TSA $A_T^{sin\phi_S \frac{\mathbf{q_T}}{M_\pi}}$ from the COMPASS data is the analysis of the influence of the target composition on the final result. The target made of solid NH_3 is submerged in liquid He and surrounded by a complex cryostat. The average target polarization throughout 2015 was $\langle P_t \rangle = 0.73$ [23]. Because of the target composition, the unpolarized part of the cross–section arises from a mixture of H and other nuclei. On the other hand the polarized part comes only from H. To correct the asymmetries for the unpolarized part of the cross section a dilution factor f is used [23]. In 2015 the average dilution factor was $\langle f \rangle = 0.18$

5.2. Data sample

The data sample consists of nine periods (W07-W15), which were collected throughout 2015. The target has two oppositely polarized cells. Each period is split into two sub–periods with reverse polarization of the target cells. The event selection proceeded in two steps. In

Table 5.1: List of cuts and number of events after each cut for the 2015 Drell–Yan data. $M_{\mu\mu}$ denotes dimuon invariant mass, R_{vert} is a radial position of the primary vertex, $P_{T,\mu}$ denotes transverse momentum of each muon in the LAB and $P_{\mu\pm}$ stands for muon momenta in the LAB.

Cuts	Events
Reconstruction of the primary vertex and check if it is in the NH$_3$ target cells	3868054
Muon trigger cut (see [23])	2979502
Bad runs rejection	2430927
$M_{\mu\mu} \in [4.3; 8.5]$ GeV/c^2	42092
$R_{vert} < 1.9$ cm	39203
$P_{T,\mu} < 7.0$ GeV/c	39132
$P_{\mu^+} + P_{\mu^-} > 190$ GeV/c	39088

this thesis the second part of the selection process is presented (whole selection process can be found in the COMPASS notes [23, 35]). Cuts and event counts are presented in Tab. 5.1.

5.3. Sivers asymmetry extraction

For the extraction of the Sivers TSA $A_T^{sin\phi_S \frac{q_T}{M_\pi}}$ we used a modified double ratio method [36]. For each period the asymmetry was extracted separately. Each period was divided into two sub–periods $p = 1, 2$, which correspond to the spin configuration of the target cells $\uparrow\downarrow, \downarrow\uparrow$. In the COMPASS setup, there are two oppositely polarized cells[1] $c = $ U, D, where U and D denote $\uparrow$ and $\downarrow$ cell polarization, respectively. The range of the azimuthal angle ϕ_S defined in Sec. 1.5 was divided into 8 bins. The modified double ratio is defined as:

$$R_{DM}^W(\phi_S) = \frac{N_{U1}^W N_{D2}^W - N_{U2}^W N_{D1}^W}{\sqrt{(N_{U1}^W N_{D2}^W + N_{U2}^W N_{D1}^W)(N_{U1} N_{D2} + N_{U2} N_{D1})}}, \tag{5.3}$$

where $N_{pc}^{(W)} = N_{pc}^{(W)}(\phi_S)$ denotes (weighted) number of events recorded in the given sub–period, cell and azimuthal angle bin (see Ref [23]).

Under the condition of a "reasonable assumption" for the ratio of the acceptances $a_{U1}(\phi_s)/a_{D1}(\phi_s) = a_{U2}(\phi_s)/a_{D2}(\phi_s)$ and the smallness of the asymmetry, the double ratio can be expressed as:

$$R_{DM}^W(\phi_S) \approx 2\langle f \rangle \langle P_t \rangle A_T^{sin\phi_S W_{\phi_S}} sin\phi_S, \tag{5.4}$$

where $A_T^{sin\phi_S W_{\phi_S}}$ denotes weighted Sivers TSA. The average target polarization P_t and the average dilution factor f were calculated for each period separately. The dilution factor for each event was taken from the pre–calculated table used for the release note [35]. Event migration between the target cells due to uncertainties in the vertex reconstruction was accounted for.

The uncertainty of the modified double ratio is defined as [23]:

$$\sigma_{R_{DM}^W}^2 = \frac{4(N_{U1} N_{D1} N_{U2} N_{D2})^2 \sum_{c,p} \sigma_{N_{cp}^W}^2}{(N_{U1} N_{D2} + N_{U2} N_{D1})^4 \sum_{c,p} N_{cp}} \sum_{c,p} \frac{1}{N_{cp}}, \tag{5.5}$$

where $\sigma_{N_{cp}^W}^2 = \sum_j W_{cpj}^2$ is the sum of the squared weights of events in a given bin.

---

[1]The cells polarization is being changed periodically during the data taking..

Table 5.2: The values of the Sivers TSAs $A_{T,i}^{sin\phi_S W_{\phi_S}}$ obtained for each period and their uncertainties $\sigma_{A,i}$.

Period	Sivers TSA $A_{T,i}^{sin\phi_S W_{\phi_S}}$	Uncertainty $\sigma_{A,i}$
W07	-0.065	0.245
W08	0.182	0.237
W09	-0.095	0.227
W10	0.057	0.228
W11	0.076	0.200
W12	0.089	0.211
W13	-0.131	0.234
W14	0.277	0.274
W15	-0.278	0.334

The weighted Sivers TSA was extracted by a fit of the modified double ratio in the 8 bins of the azimuthal angle ϕ_S with the mean value of the formula from Eq. 5.3 (in order to take into account the finite size of the bin width $\Delta\phi_S = 2\pi/8$) over each ϕ_S bin:

$$\langle R_{DM}^W \rangle (\phi_{S,i}) = \frac{2}{\Delta\phi_S} \sin\frac{\Delta\phi_S}{2} R_{DM}^W(\phi_{S,i}). \tag{5.6}$$

The values of the modified double ratios for each period and fits are shown in Fig. 5.1. The calculated values of the Sivers TSAs are presented in Tab. 5.2. Uncertainties were estimated by the fit.

5.4. Results

The asymmetries are extracted for each period separately in order to minimize effects of the experimental acceptance changes with time. The final asymmetry is calculated as statistically-weighted average of the Sivers TSAs in the periods $A_{T,i}^{sin\phi_S W_{\phi_S}}$:

$$A_T^{sin\phi_S W_{\phi_S}} = \frac{\sum_i A_{T,i}^{sin\phi_S W_{\phi_S}} \sigma_{A,i}^{-2}}{\sum_i \sigma_{A,i}^{-2}}, \tag{5.7}$$

where $\sigma_{A,i}$ is a statistical uncertainty of the asymmetry in a given period. The uncertainty of the Sivers TSA σ_A is defined as:

$$\sigma_A^2 = \frac{1}{\sum_i \sigma_{A,i}^{-2}}. \tag{5.8}$$

The result we obtained is $A_T^{sin\phi_S W_{\phi_S}} = 0.025 \pm 0.079$. It is compatible with zero within 1 σ statistical uncertainty and thus excludes any physics conclusions regarding the Sivers TSA. The planned analysis on a much enlarged data set should minimize the error of the result and thus should provide a better insight into the TMD QCD predictions and the parton angular momentum.
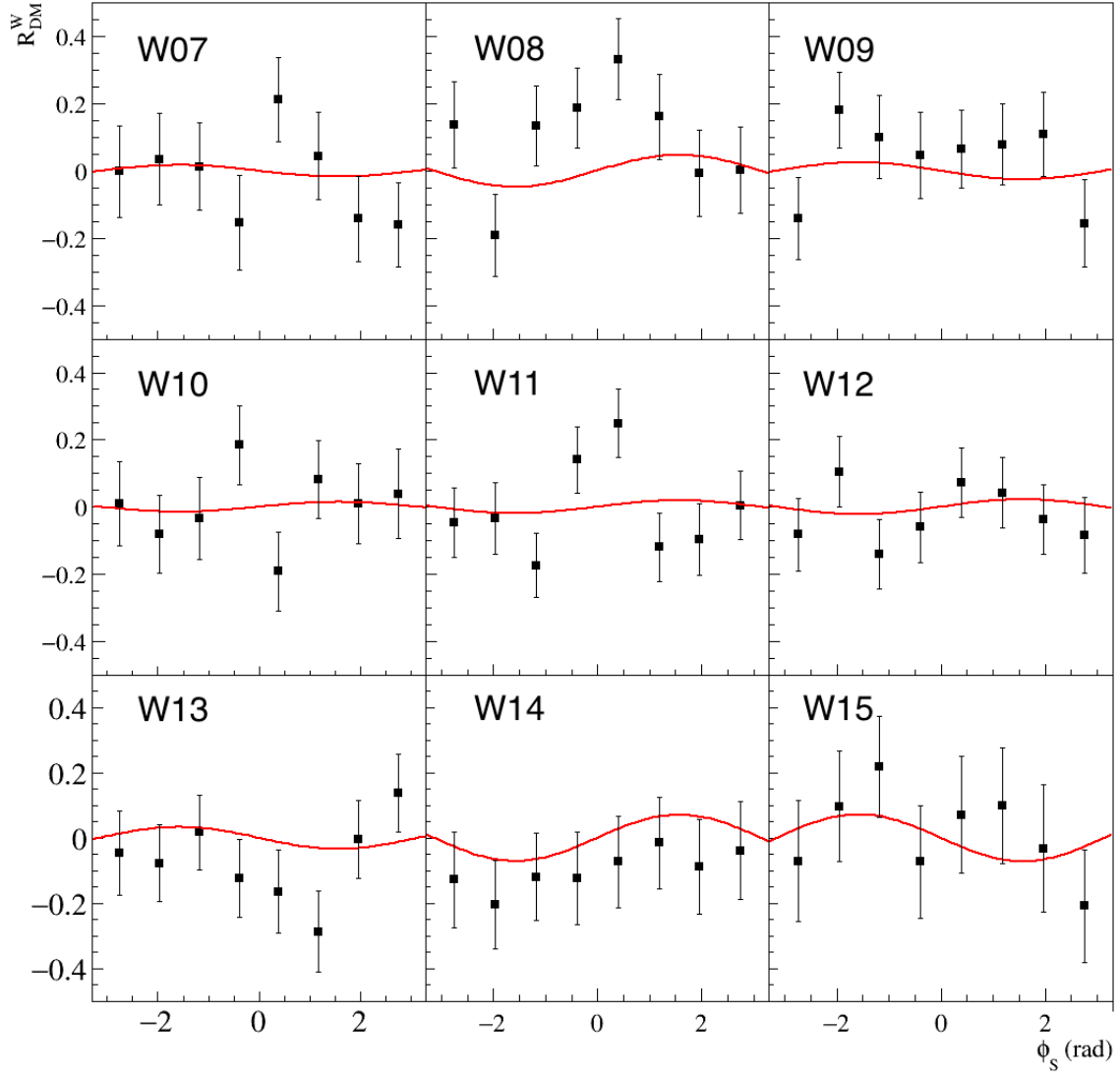
Figure 5.1: Modified double ratios as a functions of polar angle ϕ_S for all nine periods and fit functions. Points indicates values of the MDRs, red lines are the fits of the Eq. 5.6.

Chapter 6

Summary and outlook

In high energy physics the experiments and data analyses are carried by large teams (e.g. COMPASS with about 250 participants). In the beginning of my work with COMPASS I joined a small group that analyzed asymmetries extracted from 2015 data. Moreover I was entrusted a task to update a code for the COOOL plot analysis. This thesis is based on that work and tools described here are going to be used in the analysis of 2018 data.

In this thesis the study of the weighted TSAs on the COMPASS data collected in 2015 was performed. The first moment of the Boer–Mulders function $h_{1,\pi}^{\perp(1)}$ from Eq. 1.17 was extracted under the assumption that the Boer–Mulders and transversity PDFs of the quark sea are zero. The known parametrizations of the unpolarized PDFs of the proton and the pion were taken. The transversity PDF of the proton was parametrized based on the data sets extracted previously from the COMPASS results. The extracted first moment of the Boer–Mulders function weakly decreases with increasing values of x and agrees with the only existing theoretical predictions of D. Boer. Systematic checks made on the obtained $h_{1,\pi}^{\perp(1)}$ values were discussed. The results further expand our poor knowledge about the structure of the pion as the first moment of the Boer–Mulders function is one of the characteristic charges that describes this structure.

The weighted Sivers TSA $A_T^{sin\phi_S \frac{q_T}{M_\pi}}$ was extracted under the assumption for the ratio of acceptances $a_{U1}(\phi_s)/a_{D1}(\phi_s) = a_{U2}(\phi_s)/a_{D2}(\phi_s)$ and the smallness of the asymmetry. Event migration between the target cells and the finite size of the ϕ_S bin width were taken into account. The weighted Sivers TSA $A_T^{sin\phi_S \frac{q_T}{M_\pi}} = 0.025 \pm 0.079$ is compatible with zero within $1\,\sigma$ statistical uncertainty. This result demand further studies as a non-zero value of the Sivers TSA for the nucleon $A_T^{sin\phi_S \frac{q_T}{M_\pi}}$ may point towards a non-zero parton angular momentum, a missing piece in the nucleon spin puzzle.

Due to a low statistics the uncertainties of the presented results are large. Analyses of the COMPASS data collected in 2018 that can improve precision of the results are going on. The COOOL plot analysis carried by the author on the data recorded in 2018 and described here was used during the production process of the COMPASS data. All the results presented in this thesis are preliminary and wait for the official publication.

Acknowledgements

I would like to express my gratitude to Barbara Badełek, who gave me the opportunity to work with COMPASS. Her patience, help, supervision and support were invaluable.

My sincerest thanks to Bakur Parsamyan, who helped me with technical problems and led me through the analysis process.

Many thanks go to Jan Matoušek, who provided cross–check of all my results and patiently explained me the complex steps of the data analyses.

Special thanks go to Aleksander Żarnecki for his time and support.

Finally I would like to thank anybody I missed who deserves a mention.

Thank you!

Bibliography

1. Zweig, G. CERN Report No.8182/TH.401 (1964).

2. Gell-Mann, M. *Phys. Lett.* **8,** 214 (1964).

3. Feynman, R. P. *Phys. Rev. Lett.* **23,** 1415 (1969).

4. Bjorken, J. D. & Paschos, E. A. *Phys. Rev.* **185,** 1975 (1969).

5. Breidenbach, M. *et al. Phys. Rev. Lett.* **23,** 935 (1969).

6. Barber, D. P. *et al.,* PETRA Collaboration, *Phys. Rev. Lett.* **43,** 830 (1979).

7. Adams, B. *et al.,* COMPASS++/AMBER (proto-)Collaboration, arXiv:1808.00848v6.

8. Tanabashi, M. *et al.,* Particle Data Group. *Phys. Rev. D* **98,** 030001 (2018).

9. Badier, J. *et al. Z. Phys. C* **18,** 281 (1983).

10. Ashman, J. *et al.,* European Muon Collaboration, *Nucl. Phys. B* **328,** 1 (1989).

11. Gautheron, F. *et al.,* COMPASS Collaboration, (2010).

12. Arnold, S., Metz, A. & Schlegel, M. *Phys. Rev. D* **79,** 034005 (2009).

13. Kotzinian, A., COMPASS release note, February 8 (2010);
    http://wwwcompass.cern.ch/compass/notes_public/2010–2.pdf.

14. Boer, D. & Mulders, P. J. *Phys. Rev. D* **57,** 5780 (1998).

15. Kotzinian, A. & Mulders, P. *Phys. Rev. D* **54,** 1229 (1996).

16. Matoušek, J., PhD thesis (Univerity of Trieste, 2018);
    http://wwwcompass.cern.ch/compass/publications/theses/2018_phd_matousek.pdf.

17. Baum, G. *et al.,* COMPASS Collaboration,
    CERN-SPSLC-96-14, CERN-SPSLC-P-297 (1996).

18. Abbon, P. *et al.,* COMPASS Collaboration, *Nucl. Instrum. Meth. A* **577,** 455 (2007).

19. Abbon, P. *et al.,* COMPASS Collaboration, *Nucl. Instrum. Meth. A* **779,** 69 (2015).

20. Abragam, A. & Goldman, M. *Rep. Prog. Phys.* **41,** 395 (1978).

21. Airapetian, A. *et al.,* HERMES Collaboration, *Phys. Rev. Lett.* **94,** 012002 (2005).

22. Alekseev, M. G. *et al.,* COMPASS Collaboration, *Phys. Lett. B* **692,** 240 (2010).

23. Matoušek, J. *et al.* COMPASS release note, August 9 (2017);
    http://wwwcompass.cern.ch/compass/results/.html/2017/july_qTweighted_DY.

24. Rudnicki, T. *et al.* COMPASS release note, February (2019).

25. Glück, M., Reya, E. & Vogt, A. *Z. Phys. C* **53,** 651 (1992).

26. Lai, H. L. *et al.,* CTEQ Collaboration, *Eur. Phys. J. C* **12,** 375 (2000).

27. Buckley, A. *et al. Eur. Phys. J. C* **75,** 132 (2015).

28. Barry, P. C., Sato, N., Melnitchouk, W. & Ji, C.-R., JAM Collaboration. *Phys. Rev. Lett.* **121,** 152001 (2018).

29. Martin, A., Bradamante, F. & Barone, V. *Phys. Rev. D* **91,** 014034 (2015).

30. Boer, D. *Phys. Rev. D* **60,** 014012 (1999).

31. Falciano, S. *et al.,* NA10 Collaboration. *Z. Phys. C* **31,** 513 (1986).

32. Dulat, S. *et al.,* arXiv:1506.07443 (2015).

33. Anselmino, M. *et al. Phys. Rev. D* **87,** 094019 (2013).

34. Efremov, A. V. *et al. Phys. Lett. B* **612,** 233 (2005).

35. Andrieux, V. *et al.* COMPASS release note, March 23 (2017).

36. Bradamante, F. *et al.* COMPASS release note, May 18 (2016).